ELSEVIER

Chemical Geology 191 (2002) 183–207

CHEMICAL GEOLOGY
INCLUDING
ISOTOPE GEOSCIENCE

www.elsevier.com/locate/chemgeo

Textural, chemical and isotopic insights into the nature and behaviour of metamorphic monazite

Gavin Foster [a,b,*], H.D. Gibson [c], Randy Parrish [a,b], Matthew Horstwood [b], James Fraser [d], Andy Tindle [e]

[a] *Department of Geology, Leicester University, University Road, Leicester LE1 7RH, UK*
[b] *NERC Isotope Geoscience Laboratory, BGS, Nottingham NG12 5GG, UK*
[c] *Department of Earth Sciences, Carleton University, Ottawa, Ontario, Canada K1S 5B6*
[d] *Department of Earth Sciences, Oxford University, Parks Road, Oxford OX1 3PR, UK*
[e] *Department of Earth Sciences, The Open University, Walton Hall, Milton Keynes MK7 6AA, UK*

Abstract

Monazite is a mineral of choice for dating metamorphism in amphibolite- and granulite-grade metapelites. However, there exist a number of difficulties that complicate the interpretation of monazite geochronological data and prevent its application to many geological problems. The two main obstacles addressed in this contribution are firstly, the minor but significant (e.g. 1–30 Ma) dispersal in duplicate isotope dilution thermal ionisation mass spectrometry (ID-TIMS) U–Pb age data commonly recorded from a single rock, and secondly, the difficulty of attaching monazite age data to pressure and temperature information. Through a multidisciplinary approach utilising TIMS and laser ablation multicollector inductively coupled plasma mass spectrometry (LA-MC-ICPMS) isotope data, quantitative and qualitative EMP chemical analyses of monazite, and textural studies, we assess the significance of Pb loss, older components, and continuous and episodic monazite growth in the generation of dispersed age data. Three samples from the Canadian Cordillera and one sample from the Himalaya of Pakistan are examined. Each sample exhibits an age dispersion of between 1 and 12 Ma for single crystal and multi-grain TIMS U–Pb monazite age determinations. Consideration of the closure temperature for Pb diffusion in monazite and the metamorphic temperatures experienced by these samples suggests diffusive Pb loss did not play a significant part in generating this age dispersal. The LA-MC-ICPMS study indicates that an older component (< 100 Ma older than the TIMS ages) contributed to the age dispersal in three of the four samples. In all the samples however, chemical analyses identified that the majority of monazites examined exhibited significant intra-crystalline zoning in Y content. The LA-MC-ICPMS analysis of one sample that was constrained to zones of distinct Y content indicates that these zones are of distinct age. We suggest that monazite grown before the appearance of garnet and during garnet breakdown is relatively rich in Y, whereas monazite grown after garnet is relatively poor in Y. A combination of these chemical data with textural observations suggests that once monazite had entered the mineral assemblage it grew or recrystallised episodically throughout the prograde and retrograde paths of the metamorphic event. This behaviour contributes to, and in one of the samples controls, the observed age dispersal. This recognition allows the generation of pressure–temperature–time points by combining textural and chemical information of monazite with in situ age

* Corresponding author. Department of Geology, Leicester University, University Road, Leicester LE1 7RH, UK. Tel.: +44-116-252-3912; fax: +44-116-252-3918.
E-mail address: glf3@le.ac.uk (G. Foster).

PII: S0009-2541(02)00156-0

determinations, and pressure–temperature information from garnet. Thus, the episodic growth of compositionally distinct monazite throughout a metamorphic event provides the geochronologist with a very valuable chronological tool.

Keywords: Monazite; U–Th–Pb geochronology; Zoning; Metamorphism; Laser ablation; Plasma-source mass spectrometry

1. Introduction

Placing age constraints on the petrological evolution of a metamorphic rock is an essential part of determining the rates of metamorphic and tectonic processes. The mineral of choice for this is the Rare Earth Element (REE)-phosphate, monazite (e.g. Smith and Barreiro, 1990; Spear and Parrish, 1996), because it is a common accessory mineral in a variety of metamorphic rock types (Overstreet, 1967) and, importantly, is analytically relatively easy to date with the U–Th–Pb system (Parrish, 1990). Monazite has high concentrations of U and Th (Overstreet, 1967), typically low concentrations of common-Pb (Parrish, 1990), and like zircon, is highly resistant to diffusive Pb loss (Smith and Giletti, 1997; Spear and Parrish, 1996), but unlike zircon, has only a minor risk of isotopic inheritance (Parrish, 1990). However, despite these advantages, the reactions that produce and consume monazite in a metamorphic environment are poorly determined and it is often very difficult to link monazite U–Th–Pb age data to pressure, temperature and deformation information. Numerous studies have recognised the importance of such information (e.g. Bingen et al., 1996; Bea and Montero, 1999), yet the precursors of metamorphic monazite, e.g. allanite, rhabdophane, florencite, the conditions at which they breakdown to monazite, and the factors that control the extent and position of these reactions in $P–T$ space, have yet to be conclusively determined.

A review of the available literature suggests that REEs are initially transported into a sediment adsorbed to the surface of clays or as detrital heavy minerals (McLennan, 1989), and first form small grains of REE-phosphates during shallow burial (Rasmussen, 1996). Subsequent to compaction, but still at anchizone conditions, the REEs can then be redistributed to form mm-sized, nodular, grey monazite (low Th—< 2 wt.%; Milodowski and Zalasiewicz, 1991). Kingsbury et al. (1993) suggested that small grains of Th- and Ce-oxides and Ce-poor LREE-phosphates, probably equivalent to those documented in low-grade sediments by Rasmussen (1996), are the precursors of metamorphic monazite in greenschist grade metasediments. In contrast, the importance of metamorphic allanite in the production of metamorphic monazite was noted by Overstreet (1967), Smith and Barreiro (1990), Bingen et al. (1996), Simpson et al. (2000), and Ferry (2000), amongst others. In addition, allanite and apatite are often seen to replace monazite during retrograde metamorphic reactions (e.g. Finger et al., 1998; Bea and Montero, 1999), perhaps reflecting the reversal of a prograde reaction. These observations suggest that the reactions responsible for the redistribution of the REEs during burial and higher grade metamorphism are probably complex, and possibly involve several intermediate phases before the production of the Th-rich Ce-monazite that is common in amphibolite- and granulite-grade rocks.

However, before attempting to determine the reactions responsible for the growth and consumption of monazite during metamorphism there are a number of additional complexities that must first be understood. One of the most important and potentially informative complications has recently been documented by high-precision isotope dilution thermal ionisation mass spectrometry (ID-TIMS) work. Numerous ID-TIMS studies have demonstrated that the U–Th–Pb ages of single grains, and portions of grains, of metamorphic monazite are rarely identical, and instead tend to spread along concordia by as much as 30 Ma (e.g. Spear and Parrish, 1996; Bingen and van Breemen, 1998; Hawkins and Bowring, 1999). In order to investigate this problem, we have examined four samples, three from the southern Canadian Cordillera (Gibson et al., 1999) and one from the Himalaya of Pakistan (Fraser et al., 2001). Monazite U–Pb isotopic data, determined by ID-TIMS, will be presented from all four samples and the age dispersal of duplicate analyses highlighted. By examining the textural, chemical and intra- and inter-grain age variations (using LA-MC-ICPMS), we determine the processes responsible for generating the observed age variation. Our investigation strongly suggests that Pb loss plays no role in the age dispersal. The presence of significantly older monazite (30–70 Ma older than the ID-TIMS ages) was observed in three samples. In addition, in all samples, it appears that monazite growth or partial recrystallisation occurs episodically throughout the metamorphic event. These data suggest that these two processes controlled and influenced the observed age dispersal to varying degrees in all four samples. Furthermore, we demonstrate how in situ age determinations may be related to the evolution of the rock-forming mineral assemblage, and hence, to the P–T evolution of a sample.

2. Geological setting and sample description

The samples for this study were recovered from the amphibolite facies rocks of the Tertiary Himalayan and Cretaceous–Tertiary Canadian Cordilleran orogenic zones. Samples DG167, DG136, and DG122 are from the Monashee complex (Canadian Cordillera), an amphibolite facies footwall structurally overlain by an allochthon of upper amphibolite facies. All three samples are pelitic schists with assemblages of quartz, plagioclase, muscovite, biotite, garnet, kyanite, and as accessories, rutile, opaques, monazite, zircon, xenotime, and apatite. Samples DG136 and DG167 also contain allanite, with sillimanite (fibrolite) and K-feldspar also present in sample DG136. Prograde metamorphism of all these samples involved heating during tectonic thickening (Gibson et al., 1999) to upper amphibolite facies conditions (660–700 °C; Scammell, 1986). The reader is referred to Gibson et al. (1999) for a more detailed discussion of the location and tectono-thermal evolution of samples DG136, DG122 and DG167.

Sample K986 comes from sillimanite-zone rocks structurally below the Hunza Plutonic Unit of the Hunza Valley, Pakistan (see Fraser et al., 2001). This sample is a sillimanite-bearing metapelite that contains leucocratic segregations, and has an assemblage of quartz, garnet, plagioclase, sillimanite, and biotite, with accessories of monazite, zircon, apatite, and graphite. The restitic, or more pelitic component is characterised by the rock-forming mineral assemblage of biotite, garnet, sillimanite, with minor amounts of quartz and plagioclase. Prograde metamorphism occurred during burial and heating to amphibolite facies conditions (620 ± 50 °C; Fraser, 2000). The reader is referred to Fraser et al. (2001) and Fraser (2000) for a more detailed treatment of the location and tectono-thermal evolution of this sample.

3. Methodology

Monazite concentrates were obtained from all four samples from a heavy liquid treatment of disc-milled crushed whole rocks. Clear, crack-free monazite crystals were hand picked, under alcohol, from this concentrate and, from samples K986, DG122 and DG167, multi-grain fractions in the size range 100–300 μm were selected for isotope dilution U–Pb analysis. Single monazite grains of a similar size were picked and analysed from sample DG136. Prior to dissolution, all the separates were washed in warm distilled 2 N HNO_3 and acetone, spiked with a mixed ^{230}Th–^{233}U–^{235}U–^{205}Pb tracer, and dissolved in HCl (cf. Parrish et al., 1987). U–Pb analytical procedures for samples DG136, DG122, and DG167 follow those outlined in Parrish et al. (1987) and Roddick et al. (1987), using a Finnigan MAT 261 instrument at the Geological Survey of Canada. U–Pb isotopic data for sample K986 were obtained following the procedure of Noble et al. (1993) on a VG 354 mass spectrometer at the NERC Isotope Geoscience Laboratory (NIGL), Keyworth, UK. Errors were propagated from all relevant sources of uncertainty using the method of Roddick (1987). Throughout this contribution, all errors are quoted to the 2σ level of precision.

A number of monazite grains from each concentrate were also mounted in 2.5 cm diameter resin blocks and polished to expose their centres. These grain mounts were then analysed by laser ablation multi-collector inductively coupled plasma mass spectrometry (LA-MC-ICPMS). This is a relatively novel technique which was undergoing continued improvement and development during the period these samples were analysed. It is for this reason that a variety of methodologies were followed. The samples were analysed at NIGL using either a ThermoElemental Axiom or P54 multi-collector ICPMS linked to a

Merchantek 266 nm Nd/YAG laser ablation system. The analytical protocols followed for each sample are summarised in Table 1. All analyses were made by rastering the laser beam over the surface of the targeted crystal, which served to eliminate within run Pb/U and Pb/Th fractionation at the site of ablation (Fig. 1, Parrish et al., 1999; Li et al., 2001). In all analyses, ^{201}Hg or ^{202}Hg, Tl, Pb and ^{238}U or ^{232}Th isotopes were measured simultaneously on the multi-Faraday arrays of either the P54 or Axiom MC-ICPMS (nine Faraday collectors in the main array and one wide high mass Faraday collector enable a mass dispersion of up to 23%). Instrumental mass bias was determined using a simultaneously aspirated solution of Tl ($^{205}Tl/^{203}Tl$ ratio of 2.3869 calibrated to NBS981 $^{207}Pb/^{206}Pb$ of 0.914585; Todt et al., 1996) or mixed $Tl/^{235}U$ solution (e.g. Horn et al., 2000). In all cases, residual elemental fractionation was corrected for using a monazite standard of known age, the reproducibility of which is quadratically added to the internal error of each analysis (the external error in Table 1) to reflect the precision of the normalisation to the standard.

A robust common-Pb correction was only built into the analytical protocol for the analyses of monazites from sample DG167 and the compositionally constrained analyses of monazite K986 × 3. The sensitivity of the Axiom MC-ICPMS (~ 30,000 cps/ppm Pb, for this analytical protocol) enables a relatively precise measurement of ^{204}Pb to be carried out. However, the common-Pb correction was problematic due to isobaric interferences of ^{204}Hg on ^{204}Pb. In the

Table 1
Summary of LA-MC-ICPMS parameters

Sample	K986	DG136	DG122	DG167 and K986 × 3
MC-ICPMS				
Machine	P54	Axiom	Axiom	Axiom
Forward power	1250 W	1250 W	1250 W	1250 W
Cool gas flow rate	13 l/min	15 l/min	15 l/min	15 l/min
Auxillary gas flow rate	1–2 l/min	1–1.6 l/min	1–1.6 l/min	1–1.6 l/min
Injector gas flow rate	0.7–0.9 l/min	0.7–0.9 l/min	0.7–0.9 l/min	0.7–0.9 l/min
Laser				
Type	Nd/YAG 266 nm	Nd/YAG 266 nm	Nd/YAG 266 nm	Nd/YAG 266 nm
Repetition rate	10 Hz	10 Hz	10 Hz	10 Hz
Energy	< 0.1 mJ	< 0.02 mJ	< 0.02 mJ	< 0.02 mJ
Sampling method	Raster	Raster	Raster	Raster
Ablation size (x, y, z, in μm)	60 × 50 × 30	60 × 50 × 10	60 × 50 × 10	50 × 45 × 10
Scanning speed	10 μm/s	30 μm/s	30 μm/s	30 μm/s
Focus condition	constant	constant	constant	constant
Cell gas	Ar	Ar	Ar	Ar
Analytical protocol				
Isotopes analysed	Hg, Tl, Pb, ^{238}U	Hg, Tl, Pb, ^{232}Th	Hg, Tl, Pb, ^{232}Th	Hg, Tl, Pb, U
Mass bias correction	Tl	Tl	Tl	$Tl–^{235}U$
Total analyses time (min)	5	5	5	3.5
Number of integrations	50	50	50	50
Sensitivity Pb (cps/ppm)	1500	11 000	11 000	30 000
Internal precision $^{207}Pb/^{206}Pb$	1–10% 2SE	1–8% 2SE	1–8% 2SE	0.2–1% 2SE
Internal precision Pb/(U or Th)	1–2% 2SE	1–4% 2SE	1–4% 2SE	1–1.5% 2SE
External precision Pb/(U or Th)	7% 2SD	2–6% 2SD	2–6% 2SD	2–3% 2SD
Common Pb correction	No	No	No	Yes
Standard monazite	FC1	FC1 and HSA-47	FC1 and HSA-47	Manangotry
Age of standard (Ma)	54.5[a]	54.5[a] and 1875[b]	54.5[a] and 1875[b]	554[b]

[a] Parrish (1990).
[b] Parrish, unpublished data.

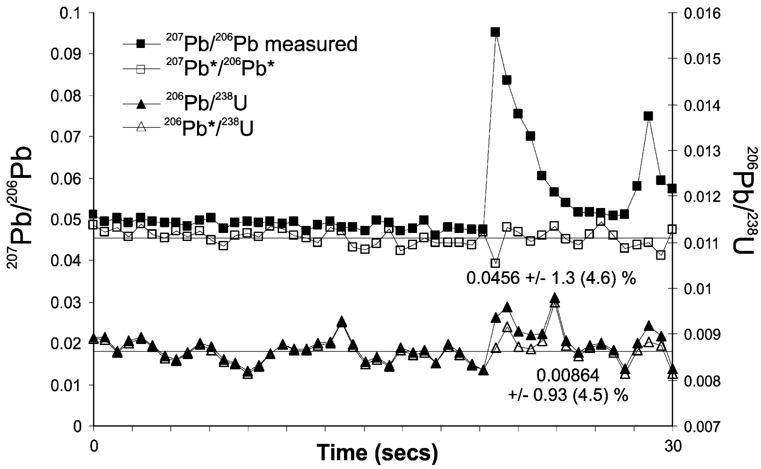

Fig. 1. Time-resolved mass-bias and fractionation corrected $^{207}Pb/^{206}Pb$ and $^{206}Pb/^{238}U$ ratios for an analysis of FC1 monazite standard (Pb* denotes that only radiogenic Pb is plotted) referenced to standard monazite HSA-47 (1875 Ma, Parrish, unpublished data). Note how the Pb/U ratio is not fractionated during the analysis. The internal and external errors after error propagation (in parenthesis) of the measured values are also shown. The ID-TIMS common-Pb corrected $^{207}Pb/^{206}Pb$ and $^{206}Pb/^{238}U$ ratios for FC1 (pegmatite, Monashee Complex, SE British Columbia) are 0.04551 ± 0.8% and 0.008776 ± 0.8% (Parrish, 1990). These values are within the external error of the common-Pb corrected LA-MC-ICPMS analysis shown here. Note that even with a point source of common-Pb ablated at around 20 s into the analysis, the common-Pb correction is still effective.

protocol followed here, an ion counter measurement of ^{201}Hg and the natural $^{204}Hg/^{201}Hg$ ratio (corrected for inverse mass bias) is used to calculate the ^{204}Hg present at mass 204 during the analysis. A common-Pb correction based on the calculated remaining ^{204}Pb and a model Pb composition (Stacey and Kramers, 1975) can then be carried out if necessary. The necessity of the correction is judged on whether the corrected $^{207}Pb/^{206}Pb$ lies outside of the internal errors of the measured ratio. The accuracy of the common-Pb correction is dependant on the amount of ^{204}Pb in relation to the radiogenic Pb. Using several crystals of known $^{207}Pb/^{206}Pb$ ratio and different Pb concentrations, an empirical estimate of the reproducibility of the correction has been generated and this is quadratically added to the internal error of the measured $^{207}Pb/^{206}Pb$. The internal error of the $^{207}Pb/^{206}Pb$ ratio for this protocol is typically in the range 0.2% (100 mV ^{207}Pb) to 1% (1 mV ^{207}Pb) 2SE, depending on the intensity of the ^{207}Pb signal. The error relating to the common-Pb correction has little effect on large signals (>10 mV ^{207}Pb), but can increase the error to as much as 8% in samples with only small amounts of Pb (< 0.5 mV ^{207}Pb). Fig. 1 illustrates the effectiveness of the common-Pb correction. However, it is commonly observed that for samples with small amounts of radiogenic Pb (< 0.5 mV ^{207}Pb) the common-Pb correction often leads to a slight over correction, either due to errors in the assumed composition of the common Pb or its measurement. For these analyses, the most robust estimate of age comes from the $^{206}Pb/^{238}U$ age, as the degree of over correction is typically minor for this system and always within analytical error.

Rastering the laser beam over the surface of the sample effectively removes the within run Pb/U fractionation by limiting the amount of ablation in the *z*-direction (see Fig. 1). Although this method limits $x-y$ spatial resolution (see Table 1), an investigation of the time resolved analysis allows any mixing in the $x-y$ dimension to be resolved to a certain extent. The degree of resolution is limited by the integration time of the analyses and the sample transfer time of the ablation cell (Bleiner and Gunther, 2001). For a number of analyses mixing has been investigated in this manner.

The accuracy of each LA-MC-ICPMS methodology was monitored at the time of analysis using

Table 2
Representative electron microprobe results for monazites from samples K986, DG136, DG122 and DG167

Name[a]	Detection limit (ppm)	K986 matb2	K986 matb7	K986 incd2	K986 incd3	DG136 mate1	DG136 mate4	DG136 mate6	DG136 mate7	DG122 matb3	DG122 matc1	DG122 matc3	DG122 matc4	DG167 inca1	DG167 inca2	DG167 mata6	DG167 mata9	Mana-ngotry this study[b]	2SD%	Mana-ngotry[c]	Mana-ngotry[d]
P_2O_5	121	30.0	30.3	30.5	30.5	29.9	30.0	30.0	30.3	29.8	30.1	30.4	29.1	29.7	29.2	29.3	29.5	25.6	1.2	25.5	26.5
SiO_2	103	0.38	0.33	0.35	0.39	0.41	0.45	0.4	0.4	0.38	0.46	0.39	0.85	0.6	1.34	1.58	0.55	2.29	2.0	2.17	2.59
ThO_2	1027	6.05	4.73	4.57	4.55	4.34	4.41	4.17	3.58	5.84	4.07	4.49	5.24	5.18	4.22	4.6	5.11	13.4	2.3	13.4	13.0
UO_2	417	0.55	0.55	0.91	0.93	0.3	0.4	0.38	0.66	0.91	0.81	0.64	0.67	0.65	0.51	0.62	0.53	0.25	10.2	0.01	0.19
Y_2O_3	239	1.92	1.8	2.84	2.96	1.32	0.22	1.28	2.46	1.42	2.13	1.7	2.06	0.42	0.38	1.08	0.73	0.21	14.2	0.14	0.17
La_2O_3	250	10.7	11.6	11.1	10.9	12.6	13.4	12.6	12.4	11.0	11.7	11.8	11.3	13.0	12.6	12.2	12.9	11.1	0.9	13.6	14.4
Ce_2O_3	302	27.1	28.4	27.4	27.3	28.0	29.4	28.2	27.4	28.1	28.9	29.2	28.0	29.7	29.5	28.4	29.3	27.7	1.2	28.3	28.1
Pr_2O_3	470	2.82	2.81	2.7	2.75	2.95	3.02	2.98	2.89	2.71	2.73	2.84	2.68	3.01	3.03	3	2.97	2.67	2.5	3.12	2.85
Nd_2O_3	350	11.2	11.2	10.9	11.0	11.1	11.3	11.5	11.1	10.8	10.8	10.9	10.5	11.2	11.2	11.6	11.3	9.60	1.1	9.75	9.33
Gd_2O_3	343	1.66	1.49	1.46	1.51	1.09	0.78	1.17	1.31	1.55	1.25	1.22	1.25	0.85	0.8	1.13	0.93	0.38	6.3	0.39	0.44
CaO	104	1.28	1.04	1.07	1.07	0.95	0.87	0.87	0.86	1.27	0.96	1.03	1.12	0.92	0.84	0.83	0.94	0.91	1.6	0.96	0.84
SmO	314	2.27	2.04	2.05	2.08	1.85	1.72	1.89	1.9	1.95	1.83	1.81	1.81	1.69	1.68	1.92	1.77	1.27	4.9	1.00	1.02
EuO	553	n.d.[e]	n.d.	n.d.	n.d.	n.d.	n.d.	n.d.	n.d.	n.d.	n.d.	n.d.	n.d.	n.d.	n.d.	n.d.	n.d.	n.d.		n.d.	n.d.
PbO	633	0.07	< d.l.[f]	< d.l.	< d.l.	< d.l.	< d.l.	< d.l.	< d.l.	< d.l.	< d.l.	< d.l.	0.07	< d.l.	< d.l.	< d.l.	< d.l.	0.35	15.3	0.29	0.31
Total[g]		96.0	96.3	95.7	95.9	94.8	96.0	95.6	95.2	95.8	95.7	96.4	94.7	96.9	95.4	96.2	96.5	95.7		98.6	99.8
Oxygens		4	4	4	4	4	4	4	4	4	4	4	4	4	4	4	4	4.00			
P		1.01	1.02	1.02	1.02	1.02	1.02	1.02	1.02	1.01	1.01	1.02	1	1	0.99	0.99	1	0.91			
Si		0.01	0.01	0.01	0.01	0.02	0.02	0.02	0.02	0.01	0.02	0.01	0.03	0.02	0.05	0.06	0.02	0.10			
Th		0.05	0.04	0.04	0.04	0.04	0.04	0.04	0.03	0.05	0.04	0.04	0.05	0.05	0.04	0.04	0.05	0.13			
U		0	0	0.01	0.01	0	0	0	0.01	0.01	0.01	0.01	0.01	0.01	0	0	0	0			
Y		0.04	0.04	0.06	0.06	0.03	0	0.03	0.05	0.03	0.05	0.04	0.04	0.01	0.01	0.02	0.02	0			
La		0.16	0.17	0.16	0.16	0.19	0.2	0.19	0.18	0.16	0.17	0.17	0.17	0.19	0.19	0.18	0.19	0.17			
Ce		0.4	0.41	0.4	0.4	0.41	0.43	0.41	0.4	0.41	0.42	0.42	0.41	0.44	0.43	0.41	0.43	0.43			
Pr		0.04	0.04	0.04	0.04	0.04	0.04	0.04	0.04	0.04	0.04	0.04	0.04	0.04	0.04	0.04	0.04	0.04			
Nd		0.16	0.16	0.15	0.16	0.16	0.16	0.16	0.16	0.16	0.15	0.15	0.15	0.16	0.16	0.16	0.16	0.14			
Gd		0.02	0.02	0.02	0.02	0.01	0.01	0.02	0.02	0.02	0.02	0.02	0.02	0.01	0.01	0.01	0.01	0.01			
Ca		0.05	0.04	0.05	0.05	0.04	0.04	0.04	0.04	0.05	0.04	0.04	0.05	0.04	0.04	0.04	0.04	0.04			
Sm		0.03	0.03	0.03	0.03	0.03	0.03	0.03	0.03	0.03	0.03	0.03	0.03	0.02	0.02	0.03	0.03	0.02			
Eu		0	0	0	0	0	0	0	0	0	0	0	0	0	0	0	0	0			
Pb		0	0	0	0	0	0	0	0	0	0	0	0	0	0	0	0	0			
Total		1.99	1.99	1.99	1.99	1.99	1.99	1.99	1.99	1.99	1.99	1.99	2.00	1.99	1.99	1.99	2.00	2.00			

[a] The letter and number prefix is the sample identifier. *Mat* denotes a grain that is not included in garnet, *inc* denotes a grain that is included within garnet. The letter suffix is a grain identifier, and the number suffix denotes the number of the analysis.

[b] Repeat analyses ($n=6$) of Managotry monazite and the reproducibility (2SD%) of these analyses.

[c] Manangotry analyses from Oelkers and Poitrasson (2002, this volume).

[d] Manangotry analyses from Scherrer, unpublished data.

[e] n.d. indicates element was not detected.

[f] < d.l. indicates analysis was below the detection limit.

[g] Totals are < 100% due to a lack of measurement of the HREEs heavier than Gd, and because of a possible systematic (2.6–3.4 wt.%) error on the La_2O_3 measurement (inference based on repeated Manangotry measurements and comparison to other laboratories).

several monazites of known age. In all instances, the measured ages were within error of the known ID-TIMS age (for example see Fig. 1).

For samples DG136, DG122 and DG167 core and rim portions of the grains (as determined optically) were analysed. For sample K986, back scattered electron (BSE) images of the mounted grains were used to guide the analyses. In addition, X-ray maps of Y, Th, and U were used to guide a number of analyses for sample DG167 and K986 (monazite K986 × 3).

The textural context of the REE-enriched phases was investigated in thin sections of the four samples. This was accomplished using the mapping function of the Cameca SX100 electron microprobe at the Open University. In addition to BSE images, element maps of Zr, Y, P, and Ce were acquired of the entire thin section at a resolution of ~ 20 μm. These maps were made using an accelerating voltage of 20 kV, a probe current of 50 nA, and a dwell time of 10 ms/pixel. The location and preliminary identification of REE-enriched species was made by overlaying the five maps using a commercial image processing program. Species identification done in this manner was later confirmed by EDS analysis on a scanning electron microscope at Leicester University. Element maps of Y, La, Th, and U in addition to BSE images were obtained on 4–10 monazites from each thin section using the Cameca SX100. Maps were made at a resolution of 0.5–1 μm (the actual resolution was probably greater than this due to the excitation volume of the electron beam, see Fig. 3) with a focussed electron beam, a probe current of 200 nA, accelerating voltage of 20 kV, and a 40 ms/pixel dwell time. Element maps were also made of selected monazite grains from the grain mounts of DG167 and K986.

Guided by the monazite element maps, quantitative WDS analysis allowed the quantification of the elemental zoning observed in the monazites of these samples. These analyses were also carried out using the Cameca SX100 electron microprobe at the Open University. All analyses were made using a 5 μm diameter electron beam, an accelerating voltage of 20 kV, and beam current of 50 nA. On-peak counting times varied from 20 to 120 s in order to optimise the detection limit which was typically less than a few hundreds of ppm (see Table 2). Careful calibration and selection of background positions ensured that interferences amongst the LREEs were minimised, although severe interference problems precluded the accurate measurement of any REE heavier than Gd. For this reason, Y has been measured as a proxy for the HREEs. The accuracy and precision of the EMP analyses was determined through repeated analyses of an inter-laboratory monazite standard (Manangotry monazite; see Table 2). It is clear from these data that the EMP analyses are both precise and accurate, with the exception of the La_2O_3 measurement that is ~ 3 wt.% low compared to the data of N. Scherrer (unpublished data) and Oelkers and Poitrasson (2002, this volume). This inaccuracy entirely accounts for the relatively low totals of the EMP analyses of this study (94–96 wt.%).

Major and trace elements for all the samples were analysed by XRF at the University of Leicester. Major elements were measured on fused glass discs using a lithium tetraborate–metaborate flux; trace elements were measured on pressed powder pellets. For major elements, the typical detection limit is 0.01% and precision is better than 0.5% at 100 times the detection limit. XRF trace element reproducibility is within 5% for international reference materials.

4. Textural investigation and whole rock chemistry

From an examination of the thin section Y, P, BSE and Zr maps, combined with EDS analysis, we have been able to determine the spatial distribution of the REE-bearing phases (including zircon) in samples K986, DG136, DG122, and DG167. Monazite, apatite, xenotime and zircon are present in all the samples, whereas allanite is only present in samples DG136 and DG167. The modal abundance of the accessory phases is shown in Table 3.

Monazite is present in all samples as a stable matrix phase at grain boundaries and as inclusions in mica and quartz. Monazite is also present as an included phase in garnet and plagioclase in samples K986, DG122, and DG167, and additionally within kyanite in samples DG122 and DG136. Notably, for sample DG167 monazite is only present in the rims of garnet. In sample DG136, monazite is not included in garnet. The modal abundance of monazite is similar for all the samples ranging from 0.01 to 0.03 modal %. Monazite in all samples has a grain size ranging

Table 3
Whole rock chemistry and accessory phase modal abundance (%) for samples discussed in text

Sample	K986	DG136	DG122	DG167
SiO_2^a	71.6	50.3	68.7	54.7
TiO_2	0.82	0.92	0.96	1.00
Al_2O_3	13.0	28.0	16.2	24.1
Fe_2O_3	5.44	11.1	7.51	8.94
MnO	0.07	0.12	0.09	0.11
MgO	1.90	2.11	2.18	2.61
CaO	2.15	1.58	0.62	2.31
Na_2O	2.13	2.12	1.00	2.08
K_2O	1.93	1.63	2.46	3.23
P_2O_5	0.05	0.13	0.08	0.37
LOI	1.11	1.61	0.24	0.76
Total	100.2	99.6	100.0	100.2
Ce^b		78	44	71
La		35	18	42
Nd		24	13	32
Th	2	16	11	15
U	3	4	3	5
Y	10	27	16	29
Zr	134	87	214	228
$Monazite^c$	0.009	0.031	0.030	0.028
Apatite	0.057	0.318	0.180	0.627
Xenotime	0.0001	0.0036	0.0060	0.0088
Zircon	0.028	0.018	0.065	0.036
Allanite	0	0.072	0	0.012

[a] Weight% oxides, Fe expressed as total Fe.
[b] Trace and REE shown as ppm.
[c] Modal abundance expressed as %.

from 10 to 300 μm, but is typically in the range of 20–150 μm.

In all samples, xenotime is considerably less abundant than the other accessory phases (0.008 to < 0.0001 modal %), and is typically of a much smaller grain size (10–20 μm). It also has a more restricted occurrence in that it is found only in garnet pressure shadows, and as inclusions in, and along the grain boundaries of, biotite, chlorite and quartz that replace garnet (Fig. 2; cf. Pyle and Spear, 1999); the significance of this observation is discussed below.

Allanite is only present in samples DG136 and DG167 where it occurs exclusively as inclusions in kyanite and garnet. In sample DG167, allanite appears to be included only in the cores of garnet and the rims of kyanite grains, whereas in sample DG136 it is present throughout garnet, but is restricted to the cores of kyanite grains. Despite its restricted occurrence, its modal abundance is relatively high (0.012 and 0.072 modal %) and its typical grain size is relatively large (20 to 200 μm long axis).

Zircon and apatite are by far the most abundant accessory phases (Table 3), and are present in all the samples investigated in this study. They are ubiquitous as included phases in garnet and other rock-forming minerals. Local high concentrations of apatite occur in bands in some of the samples, probably reflecting small-scale compositional variation. Zircon shows little systematic spatial distribution, and is likely to be predominantly of detrital origin.

The whole rock chemistry of these samples, obtained by XRF analysis, is presented in Table 3. The samples from the Canadian Cordillera (DG136, DG122, DG167) share a similar whole rock chemistry, whereas sample K986 is more Si-rich and Al-poor. The major and trace element chemistry of these samples will control and, when the phase is detrital, reflect the accessory phase assemblage. For instance, apatite and zircon abundance correlates well with the P and Zr content (respectively) of the whole rock. Similarly, the modal abundance of xenotime and monazite loosely correlate with the Y + P and Th content (respectively) of the whole rock. However, the elemental control on the occurrence of allanite is more cryptic, and is not governed simply by Ca content of the whole rock as has been observed in granitic rocks (e.g. Lee and Bastron, 1967). Instead, those samples that contain allanite have a (Ca + Al)/(Ca + Si + Al) ratio greater than 0.2; the higher the ratio the greater the modal abundance of allanite. Additional work is necessary to establish whether this is a universal relationship in pelitic rocks.

5. Chemical study

The composition of monazite in samples K986, DG136, DG122, and DG167 was investigated through a combination of elemental mapping (Y, La, U, Th) and quantitative electron microprobe analyses. Representative maps and spot analyses for monazites from these samples are shown in Figs. 3–6 and listed in Table 2, respectively. A complete set of quantitative

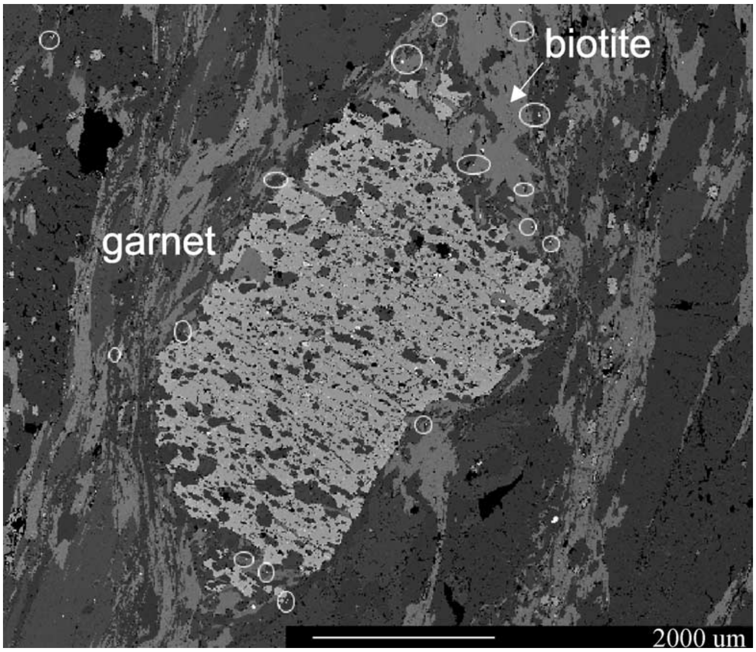

Fig. 2. The occurrence of xenotime (the circled BSE-bright dots) in sample DG167. Note how xenotime is restricted to the pressure shadows around garnet where it is breaking down to biotite. Xenotime in samples DG136, DG122, and K986 has a similar occurrence.

results is presented in the **electronic supplementary dataset** associated with this contribution (see Electronic Supplements on the journals homepage (http://www.elsevier.com/locate/chemgeo)). It should be noted that in most cases zoning visible using BSE imaging corresponds to zoning in Th and Y content.

Only monazites from sample K986 display significant BSE zoning, it is relatively minor in monazites from samples DG136 and DG122, and is absent in sample DG167. The elemental maps for monazites in sample K986 and DG122 exhibit zoning in Y, Th, and U, whereas in the other samples, only Y exhibits appreciable amounts of zoning. Monazites found in all four samples display up to three zones characterised by distinct Y content. The profiles of the grey-scale pixel values of the Y maps (see Figs. 3–6) show that the transition between the Y-zones is commonly abrupt (occurring over less than 5 μm), although in a few cases it is gradual (Fig. 5e). Typically, only the outer zone displays an euhedral shape and the inner zones are commonly rounded with embayed margins. The characteristics particular to each sample are discussed below.

The majority of monazite grains in the matrix of sample K986 have three Y-zones (Fig. 3). They typically consist of an irregularly shaped core ~ 20 μm across with a high Y content (~ 2 wt.% Y_2O_3), an inner rim ($\geq$ 20 μm) of lower Y monazite (~ 1 wt.% Y_2O_3), and an outer zone, 5 to 20 μm thick, of high Y monazite (~ 1.8 wt.% Y_2O_3; Fig. 3b). The high-Y cores are characterised by lower Th and U contents than the other zones (i.e. ~ 4.8 and 0.6 wt.% versus 5–6 and 0.5–0.8 wt.% oxides, respectively). Thorium also displays an oscillatory-type zoning within the outer two zones (Fig. 3a and c). Inclusions of monazite in garnet are similar in size to the high-Y cores of the matrix monazites, and show only the central high-Y zone and occasionally have a thin (~ 5 μm) lower Y rim (Fig. 3g). In all cases, the included monazites lack the high-Y rims. Profiles of the pixel values for the grey-scale images show that the Y zoning in the included monazites is saddle shaped (Fig. 3j). Monazites within the leucocratic segregations of this sample are rare, and those that have been identified in thin section are very similar to those described above.

The majority of monazite grains from sample DG136 also consist of three Y-zones. They are typically cored by low Y monazite (0.1 to 0.3 wt.% Y_2O_3) with an inner rim up to 20 μm thick, of higher Y monazite (~ 1.3 wt.% Y_2O_3; Fig. 4b). This is overgrown by an outer rim, typically less than 5 μm thick, of Y-enriched monazite (~ 2.5 wt.% Y_2O_3; Fig. 4b). The transition zone between the core and inner rim is characterised by a minor U enrichment (~ 0.6 wt.%; Fig. 4d). Profiles of the grey-scale pixel values show that the cores of the monazites exhibit a bell-shaped Y profile (Fig. 4e). Replacement textures, perhaps indicative of the involvement of fluids (cf. Poitrasson et al., 2000), were also found in one monazite from this sample (Fig. 4f).

Matrix monazites from sample DG122 are of three types, each displaying Y zoning. The first type (type-a; see Fig. 5a–e) consists of a core of monazite with relatively high Y (~ 1.9 wt.% Y_2O_3), and a mantle of lower Y content (~ 1.4 wt.% Y_2O_3) surrounded by a rim with higher Y content (~ 2.3 wt.% Y_2O_3). The second type (type-b; see Fig. 5f–j) has only two zones, a uniform, relatively high Y core (~ 1.8 wt.% Y_2O_3), and an even higher Y rim (~ 2.1 wt.% Y_2O_3). The third type (type-c; Fig. 5k–o) is cored by relatively low and variable Y monazite (0.4 to 0.9 wt.% Y_2O_3) overgrown by relatively high-Y monazite (~ 2.1 wt.% Y_2O_3). Thicknesses of these zones vary from ~ 20 to ~ 60 μm depending on the size of the crystal. Type-c grains tend to exhibit two zones of low Y, suggestive of grain amalgamation (see Fig. 5k–o). The grains of monazite included in garnet are typically similar in size to the cores of matrix grains and consist of one zone that is either Y-poor (i.e. type-b core) or Y-rich (i.e. type-a core). Profiles of the pixel values show that the cores of grains often exhibit a bell shaped Y zoning (Fig. 5).

Matrix monazites from sample DG167 exhibit two zones with distinct Y content. Typically grains have rims of high Y content (~ 1 wt.%) surrounding cores of relatively low Y content (0.4–0.8 wt.%). The thickness of this rim varies from several μm to ~ 25 μm. The high-Y rim is not present on monazites included in garnet, which are chemically similar to the low-Y cores of the matrix monazites (Fig. 6).

6. ID-TIMS results

The results of the ID-TIMS U–Pb study of monazites from sample K986 have been presented in detail in Fraser et al. (2001) and will not be listed here, however the pertinent information is illustrated in Fig. 7. The ID-TIMS results for samples DG136, DG122 and DG167 are presented in Fig. 7 and Table 4. All the analyses display a reversely discordant pattern, due to the presence of unsupported ^{206}Pb from ^{230}Th decay (Schärer, 1984; Parrish, 1990). No correction has been applied to compensate for this effect (cf. Schärer, 1984) because, in contrast to magmatic monazite, the Th/U ratio of the medium from which metamorphic monazite grew is unknown, and as such a correction is not applicable to metamorphic rocks. Hence, the $^{207}Pb/^{235}U$ age is thought to be the best estimate for the timing of monazite crystallisation.

6.1. Sample K986

Four monazite analyses were obtained from the pelitic, restitic portions of sample K986 and two from the more leucocratic portions. Monazites from the leucosome are typically more euhedral than those from the restite. Two monazite fractions (M1 and M2) from the more pelitic portion of this sample were strongly abraded (~ 50% of material was

Fig. 3. Chemical and BSE zoning of monazites from sample K986. (a), (b), (c), and (d), are BSE, Y, Th, and U maps of matrix monazite K986matb. The lighter the grey-scale the higher the concentration of the mapped element. (e) Is a profile of the grey-scale pixel values along line a–a′ on map (b). The resolution of these chemical maps, and consequently this profile, is approximately 5 μm. The transition between Y-zones is as sharp as the change in value encountered at the edge of the grain, suggesting that with sufficient spatial resolution the Y-zoning would consist of a series of right-angled steps. (f), (g), (h), and (i) are BSE, Y, Th and U maps of included monazite K986incc. (j) A profile of grey-scale pixel values along line a–a′ on map (g). On all maps circles denote the location of EMP quantitative analyses. The number associated with each spot is the measured composition of that spot expressed as a wt.% oxide. Note that grey-scale values are not necessarily comparable between images.

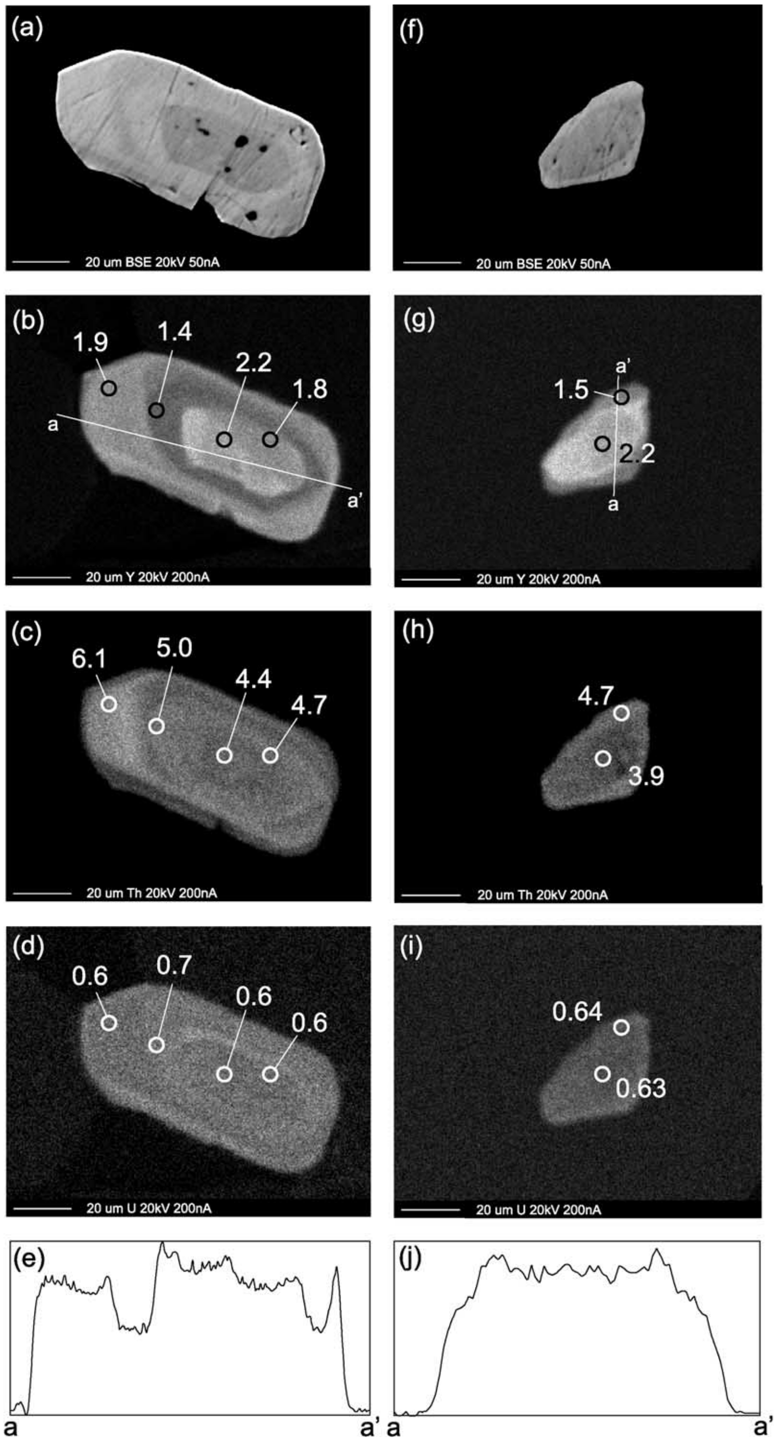
(a)
20 um BSE 20kV 50nA
(f)
20 um BSE 20kV 50nA
(b)
1.9
1.4
2.2
1.8
a
a'
20 um Y 20kV 200nA
(g)
a'
1.5
2.2
a
20 um Y 20kV 200nA
(c)
6.1
5.0
4.4
4.7
20 um Th 20kV 200nA
(h)
4.7
3.9
20 um Th 20kV 200nA
(d)
0.6
0.7
0.6
0.6
20 um U 20kV 200nA
(i)
0.64
0.63
20 um U 20kV 200nA
(e)
a
a'
(j)
a
a'

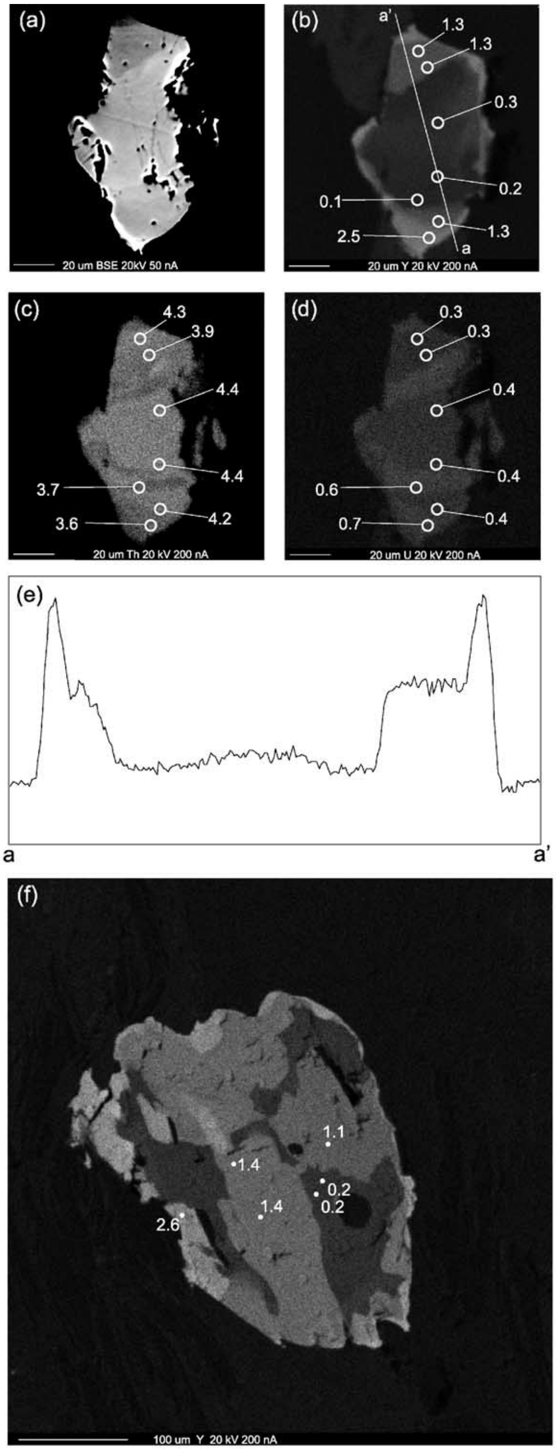

Fig. 4. Chemical and BSE zoning of monazites from sample DG136; same presentation as Fig. 3. (a), (b), (c), and (d) are BSE, Y, Th, and U maps of matrix monazite DG136mate. (e) Is a profile of the grey-scale pixel values along line a–a′ on map (b). (f) Y map of matrix monazite DG136matb; note how there appears to be extensive replacement of the various Y-zones. The resolution of these chemical maps, and consequently the profile shown in (e), is discussed in the caption of Fig. 3.

removed; Krogh, 1982). The monazite fractions from this sample exhibit ~ 10 Ma dispersion in age, with $^{207}Pb/^{235}U$ ages ranging from 53.4 ± 0.3 to 63.8 ± 0.3 Ma (see Fig. 7a). The strongly abraded fractions yield the oldest age, with both analyses within error of each other at 63.2 ± 0.4 (M2) and 63.8 ± 0.3 Ma (M1). The unabraded fractions from the pelitic portions of the sample give slightly younger $^{207}Pb/^{235}U$ ages of 63.0 ± 0.4 (M4) and 59.5 ± 0.4 Ma (M3). The euhedral monazites recovered from the more leucocratic portions of the sample give the youngest ages of 53.4 ± 0.3 Ma (M5) and 56.0 ± 0.3 Ma (M6).

6.2. Sample DG136

The four single grain monazite analyses from sample DG136 show approximately 12 million years of age dispersion, with $^{207}Pb/^{235}U$ ages ranging from 65.9 ± 0.1 to 77.5 ± 0.3 Ma (Fig. 7b).

6.3. Sample DG122

Four multigrain monazite analyses from sample DG122 plot in a cluster ranging in age from 57.8 ± 0.1 to 62.0 ± 0.1 Ma ($^{207}Pb/^{235}U$ ages) with a dispersion of ~ 4 Ma (Fig. 7c).

6.4. Sample DG167

Four multigrain analyses of sample DG167 form a much tighter cluster than the other samples investigated here and have $^{207}Pb/^{235}U$ ages varying from 59.7 ± 0.2 to 60.2 ± 0.3 Ma (Fig. 7d).

7. LA-MC-ICPMS results

The LA-MC-ICPMS data for samples DG136, DG122 and DG167 and the compositionally con-

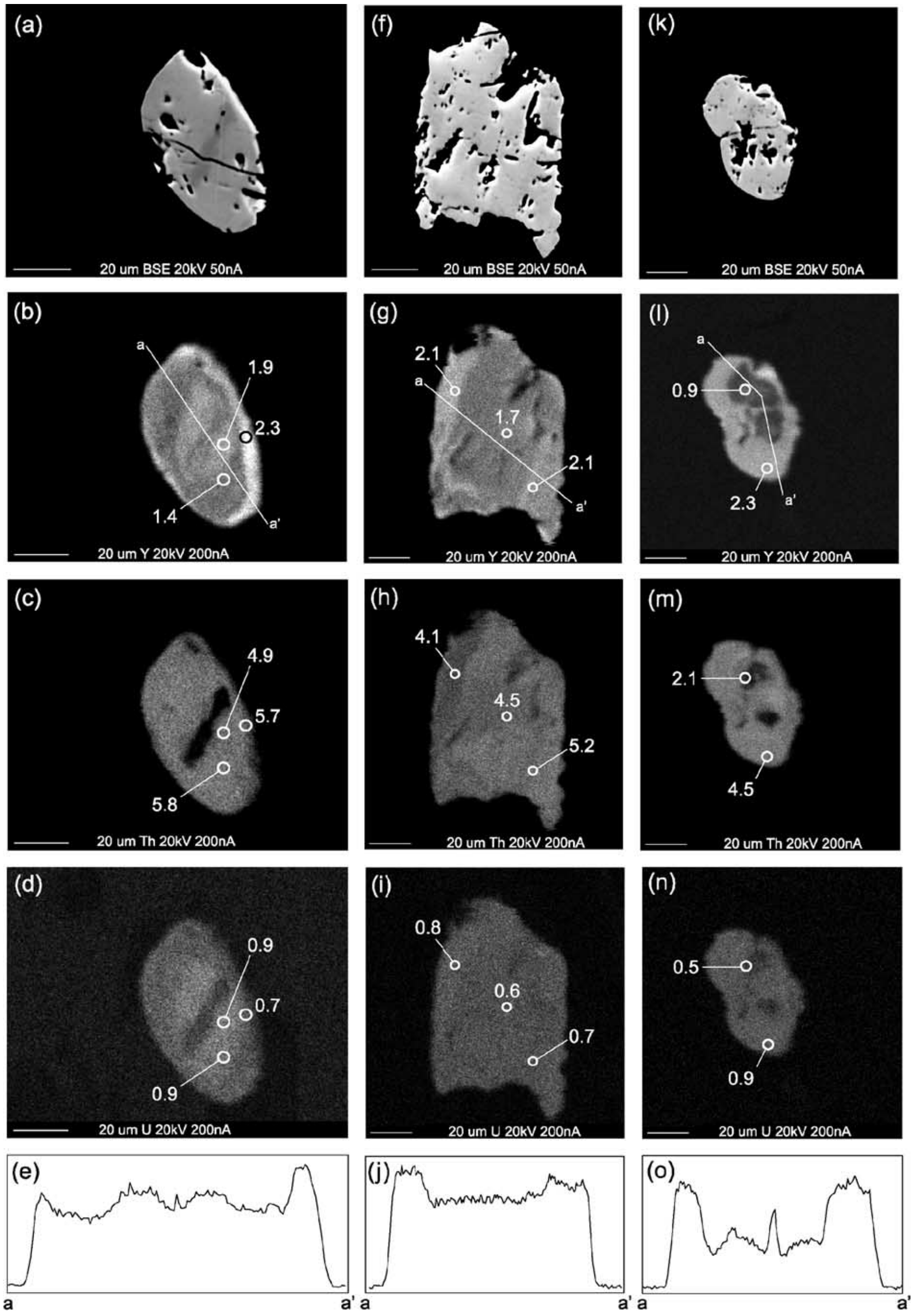

Fig. 5. Chemical and BSE zoning of monazites from sample DG122; same presentation as Fig. 3. (a), (b), (c), and (d) are BSE, Y, Th, and U maps of matrix monazite DG122matb. (e) Is a profile of the grey-scale pixel values along line a–a′ on map (b). (f), (g), (h) and (i) are BSE, Y, Th, and U maps of matrix monazite DG122matc. (j) Is a profile of the grey-scale pixel values along line a–a′ on map (g). (k), (l), (m) and (n) are BSE, Y, Th, and U maps of matrix monazite DG122mate. (o) Is a profile of the grey-scale pixel values along line a–a′ on map (l).

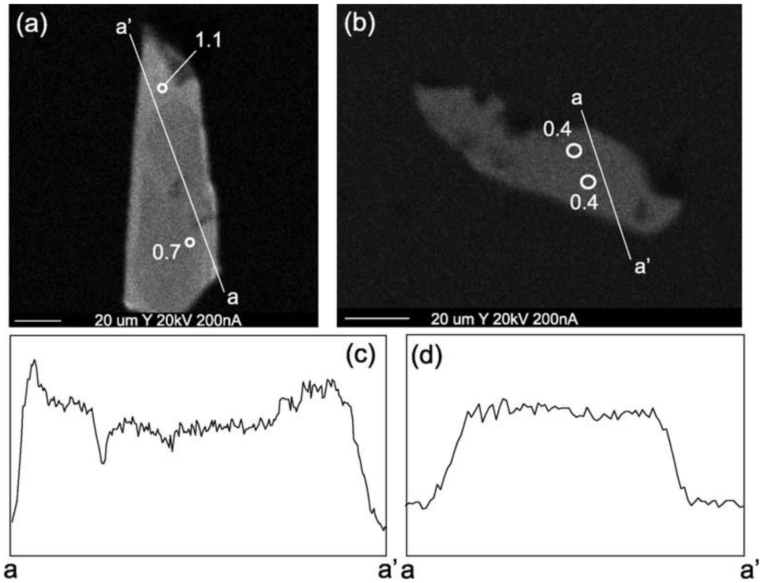

Fig. 6. Chemical and BSE zoning of monazites from sample DG167; same presentation as Fig. 3. (a) and (b) are Y maps of matrix monazite DG167mata and included monazite DG167inca, respectively. (c) Is a profile of the grey-scale pixel values along line a–a′ on map (a). (d) Is a profile of grey-scale pixel values along line a–a′ on map (b). Maps of Th, and U, and BSE images of these grains are not shown because they display no visible zoning.

strained analyses of K986 (monazite K986 × 3) are listed in Table 5. The reader is referred to Fraser et al. (2001) for a complete listing of the LA-MC-ICPMS data for the other monazites from sample K986. All LA-MC-ICPMS data are shown in Fig. 8 along with the relevant TIMS data. The compositional control on age in sample K986 is illustrated in Fig. 9.

It is clear from Fig. 8 that the LA-MC-ICPMS analyses, although markedly less precise, exhibit a much larger spread in age than the relevant TIMS ages. In samples DG136, DG167 and K986, components significantly older than the TIMS ages have been identified. In all instances, the age difference between the TIMS and LA-MC-ICPMS ages is less than 100 Ma.

The significance of the older components is not clear. It is possible that they signify the early portions of a protracted metamorphic event, although in the case of DG136, a 70 Ma long metamorphic event seems unrealistic. However, in samples DG167 and DG136, these old components are unlikely to be detrital as the deposition age of these rocks is no younger than Early Palaeozoic (Parrish, 1995). Within the northern Monashee complex, mid- to early Cretaceous ages are rare, having been reported in only one other location to the south (Crowley and Parrish, 1999). However, in the overlying allochthon, these ages are more common (e.g. Crowley et al., 2000), and thus, it seems reasonable to assume that in these two samples the older ages represent monazite grown during an earlier metamorphic event.

For sample DG136, given that many of the LA-MC-ICPMS analyses were >100 Ma, it is likely that a significant proportion of the age dispersal evident in the TIMS analyses is a result of this mixing of components. For sample DG167, the older component could be as old as 100 Ma (see Fig. 8f), but is sparsely documented (as is evident in the small spread in TIMS analyses and that only 1 out of 15 in situ analyses was largely above 60 Ma). This old component is nevertheless abundant enough to generate TIMS ages older than the LA-MC-ICPMS ages (see Fig. 8e). Repeat analyses of monazite from DG167 with an Y content of 0.4 to 0.8 wt.% (see Section 5), range in age from 54.8 ± 1.5 to 59.5 ± 1.8 Ma sug-

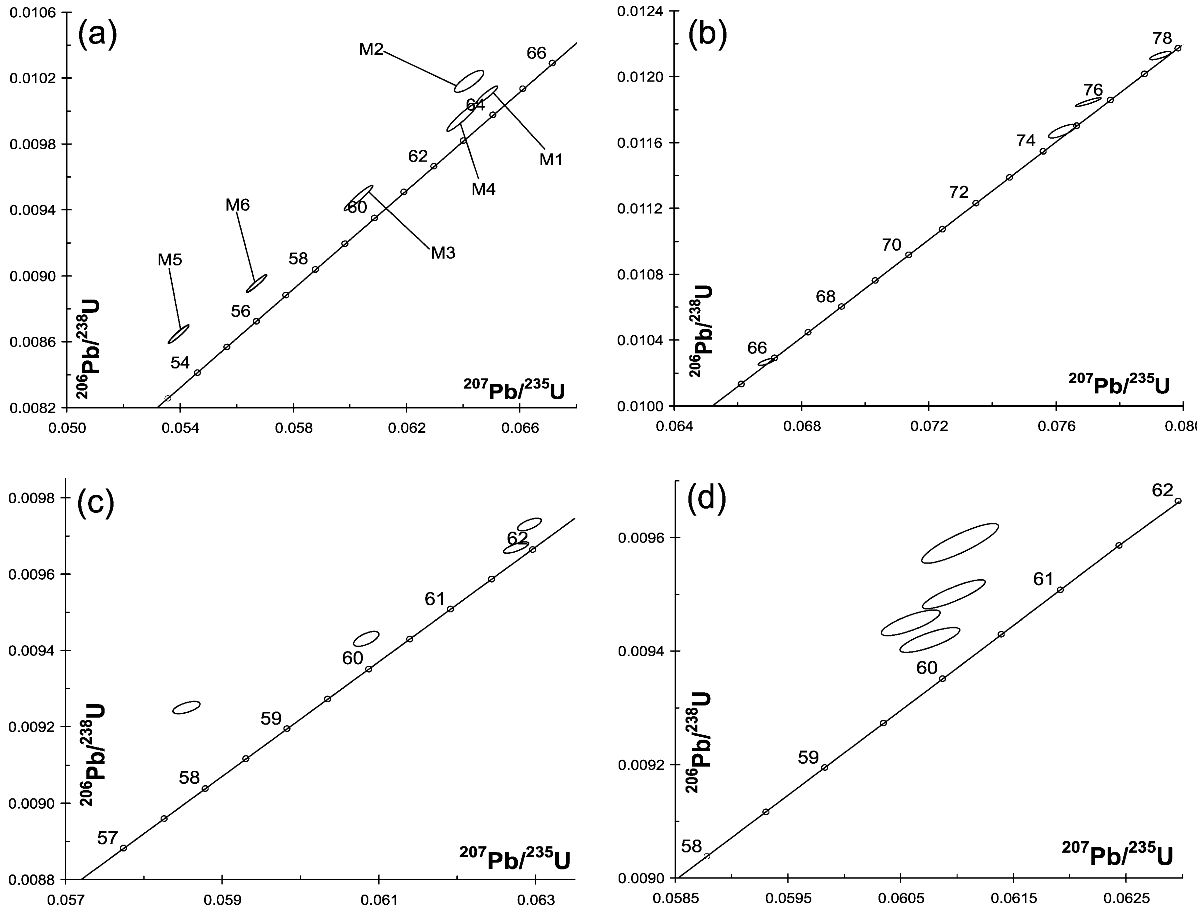

Fig. 7. Wetherill concordia plots for the TIMS U–Pb isotopic data for monazites from samples (a) K986, labelled with names of the monazite analyses—see text, (b) DG136, (c) DG122 and (d) DG167.

gesting that this Y zone grew over a few million years (see Table 5).

The analyses of monazite K986 × 3 (Figs. 8b and 9) demonstrate a definite association between age and the composition of monazite. Fig. 9 shows that the high-Y-core of monazite K986 × 3 is 86.9 ± 0.9 Ma (weighted mean, MSWD = 0.8) and the low-Y rim ranges in age from ~ 72 to ~ 59 Ma (there was no high-Y outer rim present on this monazite, see Section 5). An investigation of the time-resolved analyses indicates that K986 × 3mon5 and K986 × 3mon9 represent a mixing between two components one at ~ 60 Ma, the other at ~ 90 Ma. Fig. 9 also shows that K986 × 3mon9 is sampling low Y monazite with small isolated rafts of high-Y monazite, an observation that is consistent with this analysis being a mixture between the high-Y core and low-Y rim. Ignoring these two mixed analyses indicates that the low-Y rim probably grew from ~ 66 to ~ 59 Ma. The significance of this observation is discussed further below. The LA-MC-ICPMS ages of the low-Y rim overlap with the TIMS ages of monazites from the more pelitic portions of this sample (M1–M4). Ages as young as the youngest TIMS ages were not measured in K986 × 3.

8. Diffusive Pb loss

Diffusive Pb loss is not a common feature of monazite (Parrish, 1990), and only a few studies

Table 4
Summary of TIMS U–Pb data

Fraction	Weight[a] (mg)	U (ppm)	Pb[b] (ppm)	$^{206}Pb/^{204}Pb$[c]	Pb[d] (ng)	Th/U_{model}[e]	Isotopic ratios						Ages						Rho[f]
							$^{206}Pb/^{238}U$[g]	2σ (%)	$^{207}Pb/^{235}U$[g]	2σ (%)	$^{207}Pb/^{206}Pb$[g]	2σ (%)	$^{206}Pb/^{238}U$	2σ (Ma)	$^{207}Pb/^{235}U$	2σ (Ma)	$^{207}Pb/^{206}Pb$[h]	2σ (Ma)	
DG136																			
m1	0.030	4876	172.1	883	0.123	7.7	0.011670	0.28	0.07621	0.48	0.04736	0.42	74.8	0.2	74.6	0.4	67.4	10.0	0.77
m2	0.016	4475	151.1	1263	0.037	8.6	0.010270	0.18	0.06692	0.34	0.04724	0.24	65.9	0.1	65.8	0.2	61.4	5.7	0.75
m3	0.019	3883	139.5	1088	0.051	7.7	0.011850	0.16	0.07704	0.40	0.04717	0.32	75.9	0.1	75.4	0.3	57.8	7.6	0.92
m4	0.028	4884	173.1	1171	0.089	7.3	0.012130	0.16	0.07928	0.34	0.04738	0.26	77.7	0.1	77.5	0.3	68.4	6.2	0.75
DG122																			
m1–10	0.032	3430	128.8	3612	0.018	10.8	0.009670	0.12	0.06275	0.20	0.04705	0.14	62.0	0.1	61.8	0.1	51.8	3.3	0.76
m2–11	0.020	5601	186.3	2554	0.026	9.5	0.009430	0.16	0.06084	0.22	0.0468	0.16	60.5	0.1	60.0	0.1	39.0	3.8	0.67
m3–13	0.021	4151	182.3	2507	0.020	14.0	0.009250	0.14	0.05854	0.24	0.04589	0.20	59.4	0.1	57.8	0.1	−8.2	4.8	0.58
m4–11	0.009	9551	374.8	5067	0.010	11.4	0.009730	0.14	0.06292	0.20	0.04692	0.14	62.4	0.1	62.0	0.1	45.2	3.3	0.72
DG167																			
m1–7	0.060	5142	158.5	1851	0.101	8.6	0.009500	0.22	0.06097	0.38	0.04656	0.22	61.0	0.1	60.1	0.2	26.7	5.3	0.86
m2–7	0.050	5941	200.6	1675	0.107	9.6	0.009590	0.30	0.06103	0.46	0.04615	0.26	61.5	0.2	60.2	0.3	5.5	6.3	0.84
m3–10	0.099	4094	129.8	1762	0.136	9.0	0.009450	0.20	0.06059	0.36	0.0465	0.22	60.6	0.1	59.7	0.2	23.6	5.3	0.84
m4–10	0.111	4571	141.3	1564	0.191	8.7	0.009420	0.18	0.06077	0.36	0.04677	0.24	60.4	0.1	59.9	0.2	37.5	5.7	0.83

[a] Weighing error = 0.001 mg.
[b] Radiogenic Pb.
[c] Measured ratio, corrected for spike and Pb fractionation. For all samples, fractionation was 0.09 ± 0.03%/AMU.
[d] Total common Pb in analysis corrected for fractionation and spike.
[e] Calculated from the measured $^{208}Pb/^{206}Pb$ ratio and $^{206}Pb/^{238}U$ age.
[f] Error correlation coefficient, calculated as Ludwig (2000).
[g] Corrected for blank Pb, U, and common-Pb (Stacey and Kramers, 1975 model Pb composition equivalent to the interpreted age). Errors are standard error of the mean.
[h] Negative ages arise due to excess ^{206}Pb.

document its existence (e.g. Suzuki et al., 1994; Grove and Harrison, 1999). This is because the diffusion of Pb in monazite is slow, imparting a closure temperature in excess of ~750 °C for monazite of a typical grain size (~100 μm; Smith and Giletti, 1997; Spear and Parrish, 1996). The peak metamorphic temperatures experienced by the rocks of this study are 670–700 °C (Scammell, 1986) for the samples from the Canadian Cordillera and ~620 °C for sample K986 (Fraser, 2000). Thus, it is unlikely that monazite from these samples experienced diffusive Pb loss. The near ubiquitous presence of excess ^{206}Pb in the monazites from these samples also argues that diffusive Pb loss was insignificant (Parrish, 1990).

9. Discussion

Fig. 7 shows that ID-TIMS analyses of monazite fractions from the samples investigated here exhibit an age dispersion of 1 to 12 million years. There are four possible causes for this dispersion: (i) continuous growth and/or recrystallisation of monazite during a single metamorphic event; (ii) discontinuous growth and/or recrystallisation of monazite during a single or multiple events (either magmatic or metamorphic); (iii) diffusive Pb loss at peak metamorphic conditions from crystals grown during some previous magmatic or metamorphic event; (iv) mixing between comparatively old domains of monazite (either detrital, or monazite that formed earlier in the metamorphic cycle) and young monazite. The data presented in this contribution offer an opportunity to determine which of these scenarios is responsible for this behaviour of monazite. For instance, the possibility of Pb loss contributing to the observed age dispersal is considered unlikely as explained in the previous section. The LA-MC-ICPMS study shown in Fig. 8 indicates that the involvement of an older component in the age dispersal exhibited by samples K986, DG136 and DG167 is likely. No such component was found in sample DG122, despite numerous analyses. The age dispersal of this sample probably results from the continuous or episodic growth of monazite. The textural, compositional, and isotopic study of this sample (and K986, DG136 and DG167) is consistent with this hypothesis. The evolving chemistry of any mineral is a record of the changes in temperature, pressure and effective bulk composition (EBC; the bulk composition minus that which is locked in minerals with slow solid-state element diffusivity, such as garnet) of the rock during the growth period of the mineral in question. Because the EBC, pressure and temperature are constantly evolving with time during prograde metamorphism, minerals grown or recrystallised at different times during a metamorphic event will have subtly different compositions. Provided solid-state element diffusion is low, as is the case in monazite (e.g. Zhu and O'Nions, 1999), the resultant crystal will preserve a chemical zoning. As outlined in Section 5, chemical zoning of Th and U, the elements commonly observed to be zoned in monazite (e.g. Crowley and Ghent, 1999), is typically weak and irregular in the monazites investigated in this study (with the exception of K986). Figs. 3–6, however, indicate that Y displays considerable zoning in the majority of the mapped monazites; most monazites consist of up to three zones, each with a distinct Y content (e.g. Fig. 3b). Typically, only the outer Y-zone displays a euhedral crystal form, and the inner zones are commonly rounded and anhedral (e.g. Fig. 6a), often with embayed margins that impinge on the previous zone and have the appearance of replacement textures (e.g. Fig. 5g). In addition, the transition between zones is rarely gradual (e.g. Figs. 3–6). Figs. 8 and 9 illustrate that in samples DG167 and K986 each zone grew over several Ma, and the LA-MC-ICPMS analyses of K986 × 3 suggest that the growth was episodic, occurring during several periods when the Y content of the EBC had changed. Each growth episode may have also been preceded by a period of monazite resorption and the development of the embayment structures. Because these are features common to monazites from all the samples studied here, this method of crystallisation is probably responsible for some (K986, DG136 and DG167) or, provided considerably older components are not present, all (DG122) of the observed dispersal of U–Pb data (ID-TIMS and LA-MC-ICPMS).

Garnet and xenotime are the main reservoirs of Y in metapelitic rocks (Bea, 1996; Schwandt et al., 1996; Bea and Montero, 1999). These two minerals profoundly influence the Y content of the EBC and hence that of a growing monazite. It is therefore likely that the Y zoning displayed in the monazites from these samples reflects changes in the proportions of

Table 5
LA-MC-ICPMS isotopic data

Name	U[a] (ppm)	Th [a] (ppm)	f206%[b]	Isotopic ratios[c]								Rho[d]	Ages								Description[e]
				^{206}Pb/^{238}U	2σ %	^{207}Pb/^{235}U	2σ %	^{207}Pb/^{206}Pb	2σ %	^{208}Pb/^{232}Th	2σ %		^{206}Pb/^{238}U	2σ (Ma)	^{207}Pb/^{235}U	2σ (Ma)	^{207}Pb/^{206}Pb[f]	2σ (Ma)	^{208}Pb/^{232}Th	2σ (Ma)	
K986 × 3																					
monx3 1	2050	16,470	1.0	0.0135	1.9	0.0803	8.0	0.0431	6.7	N/A	N/A	0.2	86.5	1.6	78.4	6.3	− 162.3	167.1	N/A	N/A	high Y-core
monx3 2	1820	16,380	0.8	0.0137	1.9	0.0868	8.1	0.0459	6.7	N/A	N/A	0.2	87.8	1.7	84.6	6.8	− 6.0	162.7	N/A	N/A	high Y-core
monx3 3	2310	18,380	0.7	0.0135	2.0	0.0892	6.8	0.0479	6.2	N/A	N/A	0.3	86.5	1.7	86.8	5.9	93.2	145.9	N/A	N/A	high Y-core
monx3 4	2040	24,300	1.1	0.0099	2.2	0.0582	9.4	0.0427	7.1	N/A	N/A	0.2	63.3	1.4	57.4	5.4	− 182.3	177.3	N/A	N/A	low Y-rim
monx3 5	1310	17,650	1.3	0.0112	3.0	0.0684	8.7	0.0443	7.4	N/A	N/A	0.3	71.7	2.1	67.1	5.9	− 92.6	182.1	N/A	N/A	low Y-rim
monx3 6	1860	22,810	0.6	0.0091	1.8	0.0546	7.4	0.0433	7.4	N/A	N/A	0.2	58.6	1.1	53.9	4.0	− 150.2	182.9	N/A	N/A	low Y-rim
monx3 7	1470	22,890	1.2	0.0103	2.4	0.0628	8.5	0.0444	7.5	N/A	N/A	0.3	65.8	1.6	61.8	5.2	− 90.7	183.4	N/A	N/A	low Y-rim
monx3 8	1780	24,640	2.2	0.0095	1.9	0.0463	8.7	0.0354	7.6	N/A	N/A	0.2	60.9	1.1	46.0	4.0	− 678.5	210.2	N/A	N/A	low Y-rim
monx3 9	1170	16,480	1.6	0.0111	2.4	0.0649	9.7	0.0425	7.7	N/A	N/A	0.2	70.9	1.7	63.8	6.2	− 195.7	192.9	N/A	N/A	low Y-rim
DG136																					
mon1	N/A	3380	N/A	N/A	N/A	N/A	N/A	0.0531	5.8	0.00587	8.3	N/A	N/A	N/A	N/A	N/A	334.7	131.5	118.3	9.8	rim
mon2	N/A	3500	N/A	N/A	N/A	N/A	N/A	0.0519	2.8	0.00641	8.6	N/A	N/A	N/A	N/A	N/A	281.1	63.0	129.1	11.1	rim
mon3	N/A	59,630	N/A	N/A	N/A	N/A	N/A	0.0485	2.7	0.00328	8.2	N/A	N/A	N/A	N/A	N/A	123.1	64.0	66.1	5.4	core
mon4	N/A	5170	N/A	N/A	N/A	N/A	N/A	0.0545	8.7	0.00415	8.1	N/A	N/A	N/A	N/A	N/A	391.7	194.9	83.7	6.8	core
mon5	N/A	31,510	N/A	N/A	N/A	N/A	N/A	0.0489	2.0	0.00527	9.7	N/A	N/A	N/A	N/A	N/A	143.9	46.2	106.3	10.3	core
mon6	N/A	2490	N/A	N/A	N/A	N/A	N/A	0.0511	6.1	0.00363	9.6	N/A	N/A	N/A	N/A	N/A	246.1	141.2	73.1	7.0	core
mon7	N/A	56,160	N/A	N/A	N/A	N/A	N/A	0.0503	2.6	0.00305	8.2	N/A	N/A	N/A	N/A	N/A	207.9	60.8	61.5	5.0	core
mon8	N/A	5310	N/A	N/A	N/A	N/A	N/A	0.0467	11.7	0.00416	8.3	N/A	N/A	N/A	N/A	N/A	32.2	281.4	83.9	6.9	rim
mon9	N/A	1940	N/A	N/A	N/A	N/A	N/A	0.0497	6.5	0.00317	9.6	N/A	N/A	N/A	N/A	N/A	182.6	150.6	63.9	6.1	rim
DG122																					
mon2	N/A	38,220	N/A	N/A	N/A	N/A	N/A	0.0540	4.2	0.00285	10.3	N/A	N/A	N/A	N/A	N/A	371.2	94.0	57.4	5.9	rim
mon3a	N/A	43,500	N/A	N/A	N/A	N/A	N/A	0.0564	2.5	0.00302	10.4	N/A	N/A	N/A	N/A	N/A	469.3	56.4	60.9	6.3	rim
mon3b	N/A	45,390	N/A	N/A	N/A	N/A	N/A	0.0520	3.8	0.00314	10.4	N/A	N/A	N/A	N/A	N/A	284.4	87.3	63.3	6.6	core

mon4	N/A	29,400	N/A	N/A	N/A	N/A	N/A	0.0526	4.8	0.00319	10.5	N/A	N/A	N/A	N/A	N/A	311.2	110.2	64.5	6.8	core
mon5	N/A	24,980	N/A	N/A	N/A	N/A	N/A	0.0535	5.1	0.00290	10.3	N/A	N/A	N/A	N/A	N/A	351.8	114.2	58.4	6.0	core
mon6	N/A	26,910	N/A	N/A	N/A	N/A	N/A	0.0511	5.8	0.00333	10.3	N/A	N/A	N/A	N/A	N/A	243.5	133.6	67.1	6.9	core
DG167																					
mon1	2350	18,900	1.3	0.00889	2.0	0.0551	9.1	0.0449	8.6	N/A	N/A	0.2	57.1	1.1	54.4	5.0	− 59.0	210.5	N/A	N/A	low Y-core
mon2	2320	20,040	1.2	0.00893	2.0	0.0554	9.2	0.0450	8.7	N/A	N/A	0.2	57.3	1.2	54.8	5.0	− 55.8	211.6	N/A	N/A	low Y-core
mon4	2500	22,100	1.1	0.00903	1.9	0.0562	8.9	0.0451	8.6	N/A	N/A	0.2	58.0	1.1	55.5	5.0	− 49.1	208.1	N/A	N/A	core
mon5	1940	13,240	1.0	0.00883	2.0	0.0564	9.6	0.0463	9.0	N/A	N/A	0.2	56.7	1.1	55.7	5.4	12.2	216.6	N/A	N/A	core
mon6	2360	16,550	1.0	0.00867	1.9	0.0532	9.3	0.0445	8.8	N/A	N/A	0.2	55.7	1.1	52.7	4.9	− 81.6	216.0	N/A	N/A	core
mon7	2220	20,510	1.0	0.00920	1.9	0.0607	9.2	0.0479	8.7	N/A	N/A	0.2	59.1	1.1	59.9	5.5	92.6	205.6	N/A	N/A	core
mon9	2390	20,240	1.0	0.00915	2.0	0.0604	9.1	0.0479	8.6	N/A	N/A	0.2	58.7	1.2	59.6	5.4	95.6	203.7	N/A	N/A	core
mon10#1	3140	14,470	1.3	0.00888	3.0	0.0559	7.7	0.0457	6.6	N/A	N/A	0.4	57.0	1.7	55.2	4.3	− 19.9	160.8	N/A	N/A	low Y-core
mon10#2	2570	20,890	1.3	0.00897	3.0	0.0525	8.1	0.0425	7.2	N/A	N/A	0.4	57.5	1.7	52.0	4.2	− 198.7	179.5	N/A	N/A	low Y-core
mon10#3	2620	21,500	0.8	0.00926	3.0	0.0595	8.0	0.0465	7.0	N/A	N/A	0.4	59.5	1.8	58.6	4.7	25.6	166.8	N/A	N/A	low Y-core
mon10#4	2970	15,700	1.0	0.01174	5.4	0.0705	8.8	0.0435	6.4	N/A	N/A	0.6	75.3	4.1	69.1	6.1	− 138.2	157.6	N/A	N/A	low Y-core
mon2#1	2470	19,510	8.1	0.00854	2.7	0.0563	13.3	0.0478	7.1	N/A	N/A	0.2	54.8	1.5	55.6	7.4	88.7	167.4	N/A	N/A	low Y-core
mon2#2	2870	22,100	1.4	0.00881	2.1	0.0548	7.7	0.0451	6.9	N/A	N/A	0.4	56.5	1.2	54.2	4.1	− 49.2	167.6	N/A	N/A	low Y-core
mon2#3	3230	27,480	1.4	0.00917	2.2	0.0552	7.3	0.0436	6.7	N/A	N/A	0.5	58.9	1.3	54.6	4.0	− 130.7	164.5	N/A	N/A	low Y-core
mon2#4	3090	26,060	1.6	0.00890	2.1	0.0552	7.5	0.0450	6.7	N/A	N/A	0.4	57.1	1.2	54.6	4.1	− 55.5	163.5	N/A	N/A	low Y-core

[a] U and Th content in ppm accurate to approximately 10%. For samples DG167 and K986 [Th] is calculated.

[b] Percentage of ^{206}Pb that is common.

[c] Isotopic ratios are corrected for common-Pb except in the case of DG136 and DG122. Common-Pb correction based on a two-stage model (Stacey and Kramers, 1975) and the interpreted age of the crystal.

[d] Rho is the error correlation defined as err$^{206}Pb/^{238}U$/err$^{207}Pb/^{235}U$.

[e] Description of location of analyses determined from X-ray maps or optical examination.

[f] Negative values arise due to excess ^{206}Pb.

N/A indicates that isotope in question was not analysed.

xenotime and garnet in the evolving metamorphic mineral assemblage. Several studies have shown that as garnet-grade conditions are approached, xenotime breaks down and releases its HREE and Y to the EBC and the growing garnet (e.g. Bea and Montero, 1999; Pyle and Spear, 1999). Monazite grown before the

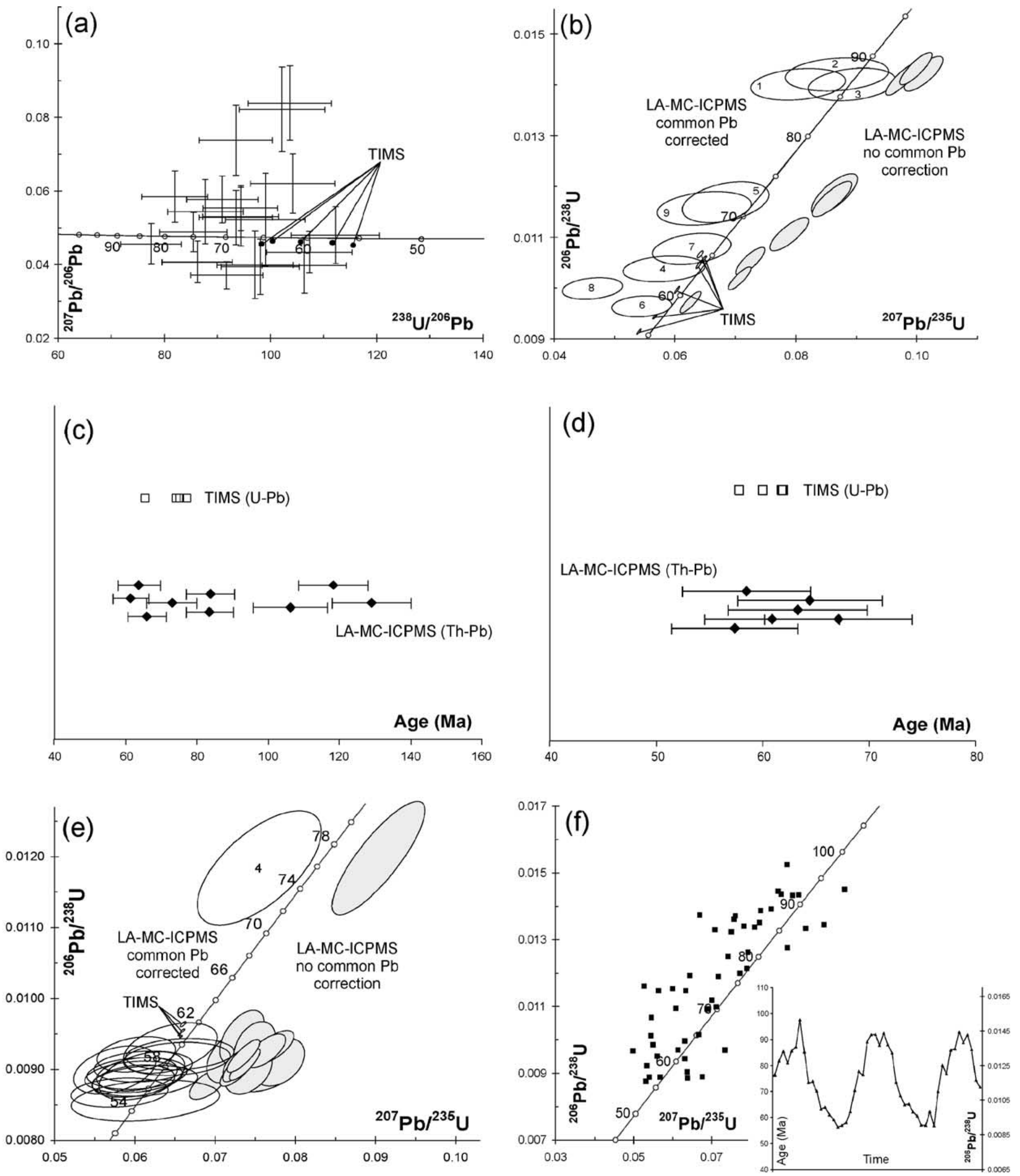

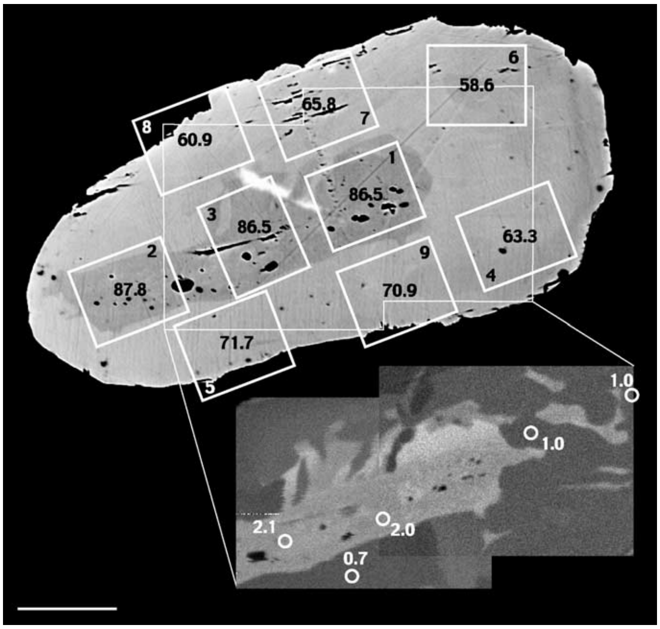

Fig. 9. BSE and Y X-ray images of monazite K986 × 3. The Y-zoning is shown in the inset. The presentation of this figure is the same as Fig. 3. Rectangles show the location of LA-MC-ICPMS analyses labelled with $^{206}Pb/^{238}U$ age in Ma. Note how the oldest ages are restricted to the analyses of the high-Y, low-BSE core of the monazite. The scale bar is 50 μm.

appearance of garnet, in equilibrium with xenotime, has a relatively high Y content. Once garnet has entered the assemblage (and xenotime has left it; Pyle and Spear, 1999; Bea and Montero, 1999; Pyle et al., 2001), the Y content of the EBC will become rapidly depleted as the available Y is partitioned into the growing garnet (Pyle and Spear, 1999). Monazite growing at this time is consequently depleted in Y. If garnet were to breakdown, Y would be released back to the EBC because the breakdown phases (plagioclase, chlorite, biotite, quartz) do not accommodate appreciable amounts of Y (Bea, 1996; Yang and Rivers, 2000). The liberated Y would be incorporated into Y-bearing minerals, such as monazite, and if sufficient Y is released, xenotime may appear (Pyle and Spear, 1999). Monazite crystallising at this time would have a relatively high Y content (Pyle and Spear, 1999; Foster et al., 2000).

The composition of the monazites investigated here reflects the redistribution of Y during the growth and breakdown of garnet. For instance, where monazite is present as an included phase throughout garnet, such as in sample K986, it is typically enriched in Y (~ 2 wt.% Y_2O_3; Fig. 3b and g). This observation suggests that these monazites grew before garnet had entered the assemblage. In sample DG167, monazite does not

Fig. 8. LA-MC-ICPMS isotopic data for samples (a) K986, (b) K986 × 3, (c) DG136, (d) DG122 (e) DG167 and (f) DG167mon10#4. Note that in (a) the data for K986 are plotted on a Terra-Wasserberg concordia diagram with no common-Pb correction applied. In (c) and (d), the ID-TIMS data are plotted as $^{207}Pb/^{235}U$ age; in all cases, the error of each analysis is smaller than the symbol. In (b) and (e), both common-Pb corrected (white ellipses) and uncorrected (grey ellipses) data are shown. The ellipse for DG167mon2#1 uncorrected is not shown as it is outside of the limits of the plot. The common-Pb corrected analyses for K986 × 3 and DG167 clearly exhibit reverse discordance; this is likely to be due to either excess ^{206}Pb, or an over correction of the common-Pb content. The $^{206}Pb/^{238}U$ ratio is typically within error of the uncorrected value and is therefore still considered to be accurate. In (b), all the analyses are labelled, whereas in (e) only mon10#4 is labelled. (f) Is the time resolved data for DG167mon10#4. Note that when the laser beam was rastered over the crystal, zones of different age were ablated. The concordia plot shows that there was mixing between at least two components, probably at ~ 55 and ~ 100 Ma.

appear as an inclusion until the growth of garnet rims; monazite inclusions in this sample are relatively low in Y (0.4–0.8 wt.% Y_2O_3; Fig. 6a and b). Thus, in this case both texture and composition suggest that monazite did not enter the assemblage until substantial amounts of garnet had already grown. Monazite is not present as an included phase in the garnets of sample DG136; matrix monazites from this sample have relatively Y-poor cores (0.1 to 0.3 wt.% Y_2O_3; Fig. 4b), indicating that portions of these grains crystallised after garnet had grown.

The rims of the majority of matrix monazite grains from all the samples are relatively enriched in Y (up to 2.5 wt.% Y_2O_3; Figs. 3–6). Notably, in all the samples garnet has partially broken down (e.g. Fig. 2). In metapelitic assemblages, garnet breakdown often occurs during cooling and decompression from amphibolite facies conditions, resulting in the production of biotite and/or chlorite (e.g. Foster et al., 2000; Vance and Mahar, 1998). It should be noted that garnet can also breakdown during the growth of staurolite along the prograde P–T path (e.g. Vance and Mahar, 1998). In the samples of this study, staurolite is not reported and garnet breakdown is attributed solely to the retrograde path of metamorphism. By breaking down, garnet releases Y to the EBC. In all the samples investigated here, the release of Y has been sufficient to induce the crystallisation of xenotime around the garnet (Fig. 2; cf. Pyle and Spear, 1999). As stated, monazite grown at this time would be Y-enriched; it therefore seems likely that the ubiquitous high-Y rims of the matrix monazites crystallised during garnet breakdown, at the end of the metamorphic event. Notably, high-Y rims are absent from all the included monazites, supporting this hypothesis.

By combining the textural observations outlined in Section 4 with the composition of the monazites discussed here and in Section 5, we are able to reconstruct the growth history of monazite and the other REE-bearing phases relative to garnet in these samples (Fig. 10). As shown in Fig. 10, once monazite has entered the assemblage it continues to grow or recrystallise, albeit episodically with possible periods of resorption (see above), throughout the metamorphic event.

The recognition that monazite with discrete composition grows/recrystallises at different times during

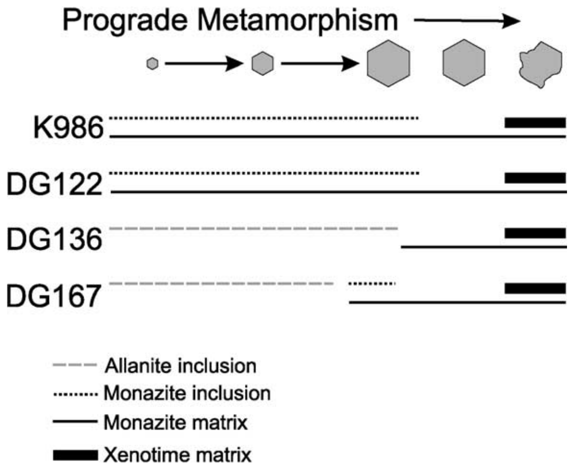

Fig. 10. Schematic diagram of the growth periods of the REE-bearing minerals relative to garnet. The hexagon represents the various growth stages of metamorphic garnet. Note that in all samples xenotime is exclusively grown during garnet breakdown at the end of prograde metamorphism. In samples K986 and DG122, monazite grew/crystallised prior to the appearance of garnet and then throughout the metamorphic event. In samples DG136 and DG167, monazite entered the assemblage relatively late, after substantial amounts of garnet had grown and allanite had left the assemblage. Note that this diagram is not taking into account the presence of old monazite in DG136 and DG167 as this monazite is interpreted to have grown during an earlier metamorphic event (see text for discussion).

the metamorphic evolution of a sample, and that one can relate monazite composition to the evolution of the rock-forming mineral assemblage in the manner described above, is extremely valuable. Provided suitable means, one can follow the approach outlined here and link in situ age analysis of chemically distinct portions of monazite, xenotime, and allanite to the rock-forming mineral assemblage, and hence with the P–T evolution of the sample in question. For instance, a combination of the in situ LA-MC-ICPMS analyses of K986 with the available compositional and textural information suggests that garnet growth occurred in this sample after ~87 Ma (the age of the high-Y cores) and before ~65 Ma (the oldest age of the low-Y rims). Similarly, in sample DG167 garnet was growing at 60–55 Ma (the age of the low Y-cores). In this way, very detailed P–T–t paths, essential for the tectono-thermal reconstruction of orogenic belts, may be constructed (cf. Foster et al., 2000). However, on a cautionary note, it is obvious from this study that unless such an approach is followed, the episodic crystallisation of metamorphic monazite can complicate the interpretation of any U–Th–Pb isotopic analysis.

These data also offer an insight into how the REEs and trace elements are re-distributed during the metamorphic evolution of a metapelite. Of particular importance is the presence of allanite in samples DG167 and DG136. Where allanite is present in these samples, i.e. in the cores of garnets and kyanite, monazite is excluded. This suggests that the LREEs, Th and U were located in allanite, rather than in monazite, prior to and during the growth of garnet and kyanite (Fig. 10). It is thus likely that allanite is the precursor for monazite in these two samples, an observation that is in accordance with several recent studies (e.g. Simpson et al., 2000). The likely precursor for monazite in samples DG122 and K986 is unknown but was also possibly allanite.

10. Conclusions

In many studies, workers have recognised that replicate metamorphic monazite U–Pb data often show a 1–30 Ma inter- and intra-crystalline age variation (e.g. Spear and Parrish, 1996; Bingen and van Breemen, 1998; Hawkins and Bowring, 1999; Foster et al., 2000). In this contribution, we have shown that there are two factors controlling the age dispersal in the samples studied. Of equal importance are the involvement of components < 100 Ma older than the main metamorphic event, and the episodic growth/recrystallisation of monazite during prograde metamorphism. It was also illustrated that Y and the HREEs in monazite appear to be key tracers that link monazite geochronological data to the petrological history of metamorphic garnet. With the proliferation of in situ dating techniques (i.e. chemical dating, LA-MC- (and quadrupole) ICPMS, ion probe), it is expected that further detailed chemical investigations of monazite will allow the reconstruction of very detailed P–T–t paths.

Acknowledgements

Nick Marsh and Tim Brewer are thanked for their assistance with the XRF data, and Rod Branson is acknowledged for help with the SEM at Leicester University. Nadim Scherrer is thanked for generously providing his unpublished EMP analyses of Manangotry monazite used in Table 2. Constructive, and in-depth reviews by Bernard Bingen, Franck Poitrasson and an anonymous reviewer significantly improved the final version of the manuscript. Franck Poitrasson is also thanked for his editorial handling of the manuscript. **[EO]**

References

Bea, F., 1996. Residence of REE, Y, Th and U in granites and crustal protoliths—implications for the chemistry of crustal melts. J. Petrol. 37 (3), 521–552.

Bea, F., Montero, P., 1999. Behavior of accessory phases and redistribution of Zr, REE, Y, Th, and U during metamorphism and partial melting of metapelites in the lower crust: an example from the Kinzigite Formation of Ivrea-Verbano, NW Italy. Geochim. Cosmochim. Acta 63 (7/8), 1133–1153.

Bingen, B., van Breemen, O., 1998. U–Pb monazite ages in amphibolite- to granulite-facies orthogneiss reflect hydrous mineral breakdown reactions: Sveconorwegian Province of SW Norway. Contrib. Mineral. Petrol. 132, 336–353.

Bingen, B., Demaiffe, D., Hertogen, J., 1996. Redistribution of rare-earth elements, thorium, and uranium over accessory minerals in the course of amphibolite to granulite-facies metamorphism—the role of apatite and monazite in orthogneisses from Southwestern Norway. Geochim. Cosmochim. Acta 60 (8), 1341–1354.

Bleiner, D., Gunther, D., 2001. Theoretical description and experimental observation of aerosol transport processes in laser ablation inductively coupled plasma mass spectrometry. J. Anal. At. Spectrom. 16, 449–456.

Crowley, J.L., Ghent, E.D., 1999. An electron microprobe study of the U–Th–Pb systematics of metamorphosed monazite: the role of Pb diffusion versus overgrowth and recrystallisation. Chem. Geol. 157, 285–302.

Crowley, J.L., Parrish, R.R., 1999. U–Pb isotopic constraints on diachronous metamorphism in the northern Monashee complex, southern Canadian Cordillera. J. Metamorph. Geol. 17, 483–502.

Crowley, J.L., Ghent, E.D., Carr, S.D., Simony, P.S., Hamilton, M.A., 2000. Multiple thermotectonic events in a continuous metamorphic sequence, Mica Creek area, southeastern Canadian Cordillera. Geol. Mater. Res. 2 (2), 1–44.

Ferry, J.M., 2000. Patterns of mineral occurrence in metamorphic rocks. Am. Mineral. 85, 1573–1588.

Finger, F., Broska, I., Roberts, M.P., Schermaier, A., 1998. Replacement of primary monazite by apatite–allanite–epidote coronas in an amphibolite facies granite gneiss from the eastern Alps. Am. Mineral. 83 (3–4), 248–258.

Foster, G., Kinny, P., Prince, C., Vance, D., Harris, N., 2000. The significance of monazite U–Th–Pb age data in metamorphic assemblages; a combined study of monazite and garnet chronometry. Earth Planet. Sci. Lett. 181, 327–340.

Fraser, J., 2000. The structural and metamorphic evolution of the deep crust in Hunza Karakoram, Pakistan. PhD Thesis, St Annes College, Oxford University, Oxford, 440 pp.

Fraser, J., Searle, M., Parrish, R.R., Noble, S., 2001. Chronology of deformation, metamorphism and magmatism in the southern Karakoram Mountains. Geol. Soc. Amer. Bull. 113 (11), 1443–1455.

Gibson, H.D., Brown, R.L., Parrish, R.R., 1999. Deformation-induced inverted metamorphic field gradients: an example from the southeastern Canadian Cordillera. J. Struct. Geol. 21, 751–767.

Grove, M., Harrison, T.M., 1999. Monazite Th–Pb age depth profiling. Geology 27 (6), 487–490.

Hawkins, D.P., Bowring, S.A., 1999. U–Pb monazite, xenotime, and titanite geochronological constraints on the prograde to post-peak metamorphic thermal history of Paleoproterozoic migmatites from the Grand Canyon, Arizona. Contrib. Mineral. Petrol. 134, 150–169.

Horn, I., Rudnick, R.L., McDonough, W.F., 2000. Precise elemental and isotope ratio determination by simultaneous solution nebulization and laser ablation-ICP-MS: application to U–Pb geochronology. Chem. Geol. 164, 281–301.

Kingsbury, J.A., Miller, C.F., Wooden, J.L., Harrison, T.M., 1993. Monazite paragenesis and U–Pb systematics in rocks of the eastern mojave desert, California, USA: implications for thermochronology. Chem. Geol. 110, 147–167.

Krogh, T.E., 1982. Improved accuracy of U–Pb zircon ages by the creation of more concordant systems using an air abrasion technique. Geochim. Cosmochim. Acta 46, 637–649.

Lee, D.E., Bastron, H., 1967. Fractionation of rare-earth elements in allanite and monazite as related to geology of the Mt. Wheeler mine area, Nevada. Geochim. Cosmochim. Acta 31, 339–356.

Li, X.-H., Liang, X.-R., Sun, M., Guan, H., Malpas, J.G., 2001. Precise $^{206}Pb/^{238}U$ age determinations on zircons by laser ablation microprobe-inductively coupled plasma-mass spectrometry using continuous linear ablation. Chem. Geol. 175, 209–219.

Ludwig, K.R., 2000. Users manual for Isoplot/Ex v.2.3. A Geochronological Toolkit for Microsoft Excel. Berkeley Geochronological Center Special Publication No. 1a, Berkeley, CA.

McLennan, S.M., 1989. Rare earth elements in sedimentary rocks: influence of provenance and sedimentary processes. In: Lipin, B.R., McKay, G.A. (Eds.), Geochemistry and Mineralogy of the Rare Earth Elements. Mineralogical Society America, Reviews in Mineralogy, Washington, pp. 169–200.

Milodowski, A.E., Zalasiewicz, J.A., 1991. Redistribution of Rare Earth elements during diagenesis of turbidite/hemipelagite mudrock sequences of Llandovery age from central Wales. In: Morton, A.C., Todd, S.P., Houghton, P.D. (Eds.), Developments in Sedimentary Provenance Studies. Geological Society London, Special Publication, London, pp. 101–124.

Noble, S., Tucker, R.D., Pharoah, T.C., 1993. Lower Paleozoic and Precambrian igneous rocks from Eastern England, and their bearing on late Ordovician closure of the Tornquist Sea—constraints from U–Pb and Nd isotopes. Geol. Mag. 130 (6), 835–846.

Oelkers, E.H., Poitrasson, F., 2002. An experimental study of the dissolution stoichiometry and rates of natural monazite as a function of temperature from 50 to 230 °C and pH from 1.5 to 10. Chem. Geol., 191, 73–87 (this volume).

Overstreet, W.C., 1967. The geological occurrence of monazite. U.S. Geol. Surv. Prof. Pap. 530, 1–327.

Parrish, R.R., Roddick, J.C., Loveridge, W.D., Sullioan, R.W., 1987. Uranium-Lead analytical techniques at the geochronology laboratory. Geol. Surv. Can. Pap. 87-2, 3–7.

Parrish, R.R., 1990. U–Pb dating of monazite and its application to geological problems. Can. J. Earth Sci. 27 (11), 1431–1450.

Parrish, R.R., 1995. Thermal evolution of the southeastern Canadian Cordillera. Can. J. Earth Sci. 32 (10), 1618–1642.

Parrish, R.R., et al., 1999. Laser ablation plasma ionization multicollector mass spectrometry: a new method for intracrystal uranium–thorium–lead geochronology using micro-sampling techniques. Ninth Annual Goldschmidt Conference. LPI Contribution No. 971, Lunar and Planetary Institute, Houston, p. 219.

Poitrasson, F., Chenery, S., Shepherd, T.J., 2000. Electron microprobe and LA-ICP-MS study of monazite hydrothermal alteration: implications for U–Th–Pb geochronology and nuclear ceramics. Geochim. Cosmochim. Acta 64 (19), 3283–3297.

Pyle, J., Spear, F.S., 1999. Yttrium zoning in garnet: coupling of major and accessory phases during metamorphic reactions. Geol. Mater. Res. 1 (6), 1–49.

Pyle, J.M., Spear, F.S., Rudnick, R.L., McDonough, W.F., 2001. Monazite–xenotime–garnet equilibrium in metapelites and a new monazite–garnet thermometer. J. Petrol. 42 (11), 2083–2107.

Rasmussen, B., 1996. Early diagenetic REE-phosphate minerals (florencite, gorgeixite, crandallite, and xenotime). Am. J. Sci. 296, 601–632.

Roddick, J.C., 1987. Generalised numerical error analysis with applications to geochronology and thermodynamics. Geochim. Cosmochim. Acta 51, 2129–2135.

Roddick, J.C., Loveridge, W.D., Parrish, R.R., 1987. Precise U/Pb dating of zircon at the sub-nanogram Pb level. Chem. Geol. 66, 111–121.

Scammell, R.J., 1986. Stratigraphy, structure and metamorphism of the north flank of the Monashee complex, southeastern British Columbia: a record of the Proterozoic crustal thickening. MSc. Thesis, Carleton University, Ottawa, Canada.

Schärer, U., 1984. The effect of initial ^{230}Th disequilibrium on young U–Pb ages: the Makalu case, Himalaya. Earth Planet. Sci. Lett. 67, 191–204.

Schwandt, C.S., Papike, J.J., Shearer, C.K., 1996. Trace element zoning in pelitic garnet of Black Hills, South Dakota. Am. Mineral. 81, 1195–1207.

Simpson, R.L., Parrish, R.R., Searle, M.P., Waters, D.J., 2000. Two episodes of monazite crystallisation during metamorphism and crustal melting in the Everest region of the Nepalese Himalaya. Geology 28 (5), 403–406.

Smith, H.A., Barreiro, B., 1990. Monazite U–Pb dating of staurolite grade metamorphism in pelitic schists. Contrib. Mineral. Petrol. 105, 602–615.

Smith, H.A., Giletti, B.J., 1997. Pb diffusion in monazite. Geochim. Cosmochim. Acta 51 (5), 1047–1055.

Spear, F.S., Parrish, R.R., 1996. Petrology and cooling rates of the Valhalla complex, British Columbia, Canada. J. Petrol. 37 (4), 733–765.

Stacey, J.S., Kramers, J.D., 1975. Approximation of terrestrial lead isotope evolution by a two-stage model. Earth Planet. Sci. Lett. 26, 207–221.

Suzuki, K., Adachi, M., Kajizuka, I., 1994. Electron microprobe observations of Pb diffusion in metamorphosed detrital monazites. Earth Planet. Sci. Lett. 128, 391–405.

Todt, W., Cliff, R.A., Hanser, A., Hofmann, A.W., 1996. Evaluation of a ^{202}Pb–^{205}Pb double spike for high-precision lead isotope analysis, Earth Processes: reading the isotopic code. Am. Geophys. Union, Wash., pp. 429–437.

Vance, D., Mahar, E., 1998. Pressure–temperature paths from P–T pseudosections and zoned garnets: potential, pitfalls and examples from the Zanskar Himalaya, NW India. Contrib. Mineral. Petrol. 132, 225–245.

Yang, P., Rivers, T., 2000. Trace element partitioning between coexisting biotite and muscovite from metamorphic rocks, Western Labrador: structural, compositional and thermal controls. Geochim. Cosmochim. Acta 64 (8), 1451–1472.

Zhu, X.K., O'Nions, R.K., 1999. Zoning of monazite in metamorphic rocks and its implications for high temperature thermochronology: a case study from the Lewisian Terrane. Earth Planet. Sci. Lett. 171, 209–220.